Aus dem Neurozentrum
Klinik für Neuroradiologie
des Universitätsklinikums Freiburg im Breisgau

Spatial metabolic pattern of the human brain in health and disease

INAUGURAL-DISSERTATION
zur
Erlangung des Medizinischen Doktorgrades
der Medizinischen Fakultät
der Albert-Ludwigs-Universität Freiburg im Breisgau

Vorgelegt 2021
von Pamela Heiland, geb. Franco Jiménez
geboren in Bogotá, Kolumbien

Dekan: Prof. Dr. Lutz Hein

1. Gutachterin: Prof. Dr. Irina Mader
2. Gutachter: Prof. Dr. Oliver Schnell

Jahr der Promotion: 2022

Dedication

For my parents and grandparents for their unparalleled encouragement in every step of my life.

For my husband for his unconditional love, support and patience.

For my son for lighting up our lives.

Para mi familia.

Table of contents

List of figures

List of tables

Abbreviations

^{1}H MRS	Proton magnetic resonance spectroscopy
2-HG	2-hydroxyglutarate
α-KG	α-ketoglutarate
AI	Artificial intelligence
Ala	Alanine
Asp	Aspartate
AUC	Area under the curve

ATRX	A-thalassemia/mental retardation syndrome X-linked
Cho	Choline
CIMP	CpG island methylator phenotype
CNS	Central nervous system
Cr	Creatine
CSI	Chemical shift imaging
DNET	Dysembryoplastic neuroepithelial tumour
DTI	Diffusion tensor imaging
EGFR	Epidermal growth factor receptor
FCD	Focal cortical dysplasia
FLAIR	Fluid attenuated inversion recovery
fMRI	Functional magnetic resonance imaging
GABA	Gamma-Aminobutyric acid
GPC	Glycerophosphocholine
Gln	Glutamine
Glu	Glutamic acid
HDBSCAN	Hierarchical density-based spatial clustering
ICH	Intracranial haemorrhage
IDH	Isocitrate dehydrogenase
KDM	Lysine demethylase
Lac	Lactate
LDA	Linear discriminant analysis
LOH	Loss of heterozygosity
MGMT	O (^{6})-Methylguanine-DNA methyltransferase

mIns	Myo-inositol
MM	Macromolecules
MRI	Magnetic resonance imaging
MRS	Magnetic resonance spectroscopy
MS	Multiple sclerosis
NAA	*N*-acetyl aspartate
NAM	Normal appearing matter
NHL	Non-Hodgkin lymphoma
NSCLC	Non-small cell lung cancer
O^6-MG	O^6-methylguanine
PCA	Principal component analysis
ppm	Parts per million
PTEN	Phosphatase and tensin homolog protein
ROI	Region of interest
SNN	Spiking neural network
SPATA	SPAtial Transcriptomic Analysis
SPORT	Spectroscopic Prediction Of bRain Tumours
TARQUIN	Totally Automatic Robust Quantitation in NMR
TE	Echo time
TET	Ten-eleven translocation methylcytosine dioxygenase
TERT	Telomerase reverse transcriptase
TI	Inversion time
TP53	Tumour protein P53
TR	Repetition time

UMAP	Uniform Manifold Approximation and Projection
VOI	Volume of interest
WHO	World health organization

1. Introduction

1.1. Epidemiology of brain tumours

Brain tumour cases have surged in recent years worldwide. It has been reported that malignant brain tumours have a global incidence of 4.25 cases per 100.000 persons-years. In Europe the incidence has been calculated at 6.76, in the United States of America at 6.48 and in Latin America at 5.25 cases per 100.000 persons-years. In Africa and South East Asia, the incidence is the lowest with 2.81 and 3.27 cases per 100.000 persons-years[1–3]. The highest death rates due to central nervous system (CNS) tumours were reported in western Europe, southeast Asia and Latin America, although the USA alone was among the countries with the highest death rates[3].

Figure 1

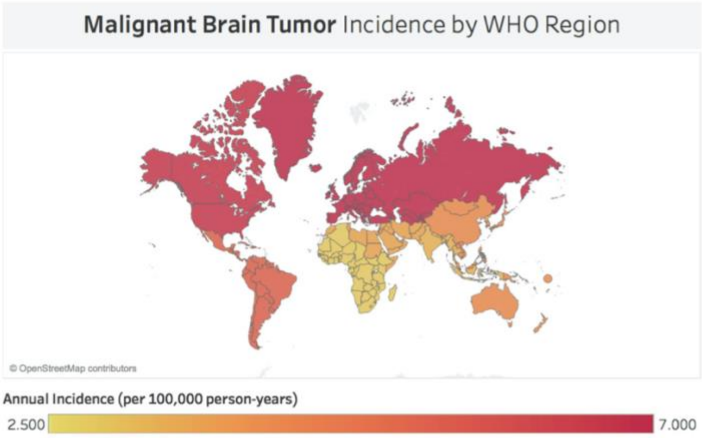

Global incidence and regional variations of malignant brain tumours. Taken from[1].

Malignant brain tumours have a tendency to be more frequent in men and in advanced age, with the highest rate at 65-80 years[3].

Figure 2

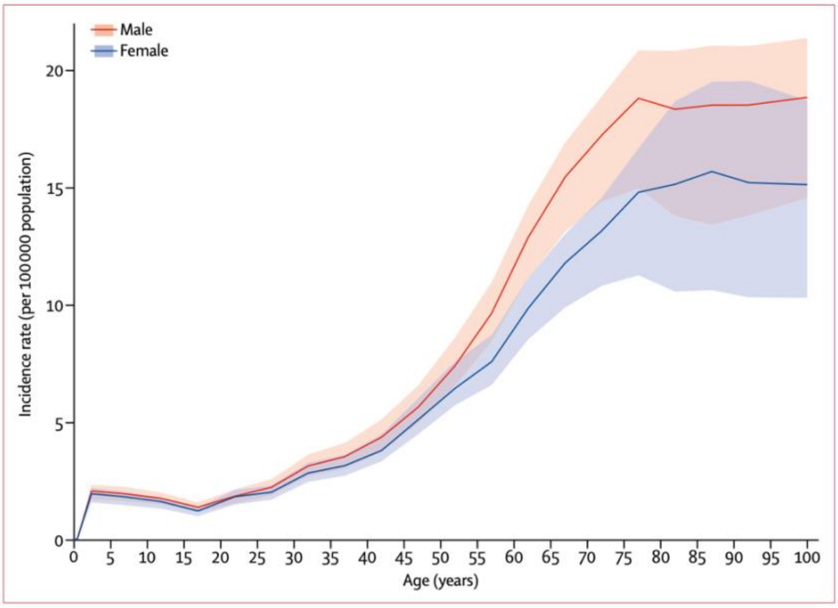

Global age-standardised incidence rate per 100.000 persons-years of brain tumours by sex and age. Taken from[3].

With respect to tumour subtypes, meningiomas are the most common tumours of the central nervous system at 37.2% and of all benign tumours**.** Glioblastoma is the most frequently diagnosed malignant tumour representing 14.6%. The frontal lobe is the prevalent location for any brain tumour[4,5].

Figure 3

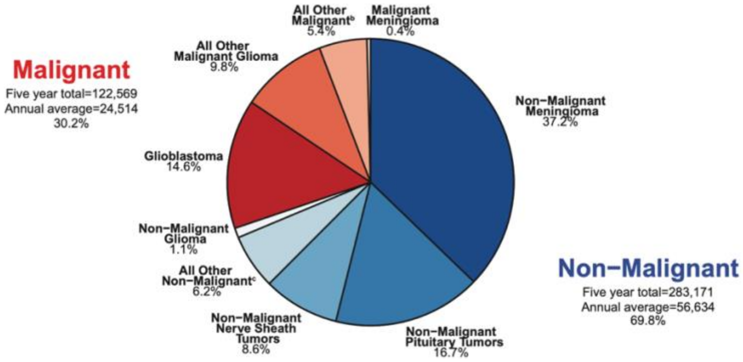

Distribution of the brain tumours (primary and other). Taken from [4].

Figure 4

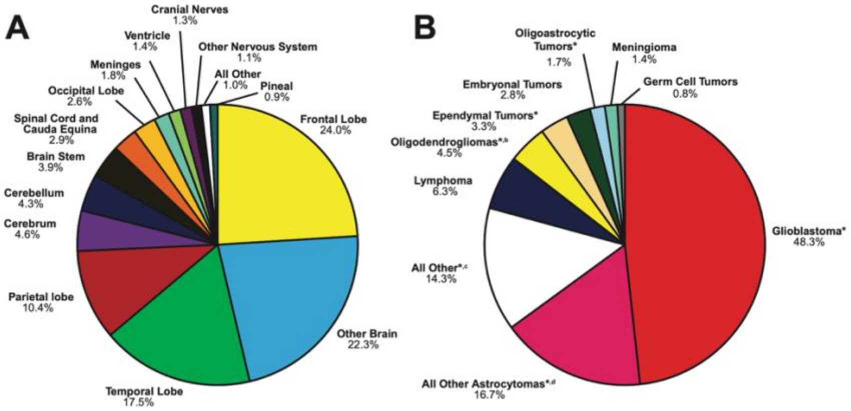

A. Distribution of anatomical invasion of brain tumours. B. Distribution of malignant brain tumours. Taken from [4].

1.2. Glioma

1.2.1. Diagnosis

Gliomas are tumours that vary in the clinical presentation, low-grade tumours have a gradual growth, and patients usually have a prolonged course of disease**,** while high-grade tumours present with acute symptomatic due to the rapid and uncontrolled growth. Symptoms for both types of tumours include focal neurological deficits (in 68% of patients, with motor weakness being the leading symptom with 47% frequency), headache (54%) and seizures (26%), which can arise focally, then generalize secondarily and are more common in low-grade gliomas [6]. High-grade tumours often present with signs of increased intracranial pressure. In addition, different syndromes may arise depending on the affected area of the brain[7].

Magnetic resonance imaging (MRI) is the gold standard for diagnosis of gliomas. Native and contrast-enhanced T1-weighted along with T2- and T2-FLAIR-weighted sequences should be the primary sequences obtained as they deliver high precision imaging of the brain’s anatomy and are essential for delineating the tumour’s boundaries and planning the surgical treatment. Functional neuroimaging techniques (such as functional magnetic resonance imaging (fMRI) and diffusion tensor imaging (DTI)) might be necessary for detailed depiction of surgically and functionally relevant structures such as the pyramidal and sensory tracts, the optic pathway and so forth. Magnetic resonance spectroscopy is a technique with which the biochemical composition of tissues can be assessed. Further details and explanations on this topic and its relevance in neuro-oncology are described below.

Figure 5

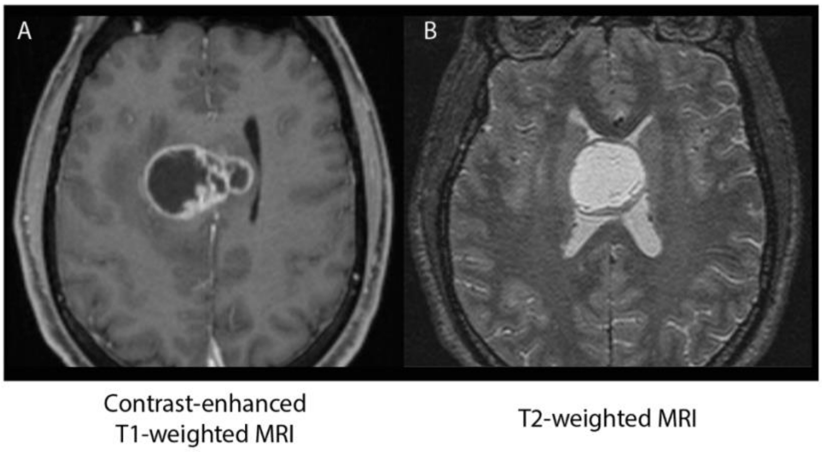

MRI from a patient with an IDH-wildtype glioblastoma. A. Contrast-enhanced axial T1-weighted MRI, depicting a central necrotic tumour with a contrast–enhancing rim. B. T2-weighted axial MRI where the tumour appears hyperintense with only little oedema. The images were taken at the Department of Neuroradiology from the Medical Centre – University of Freiburg.

Figure 6

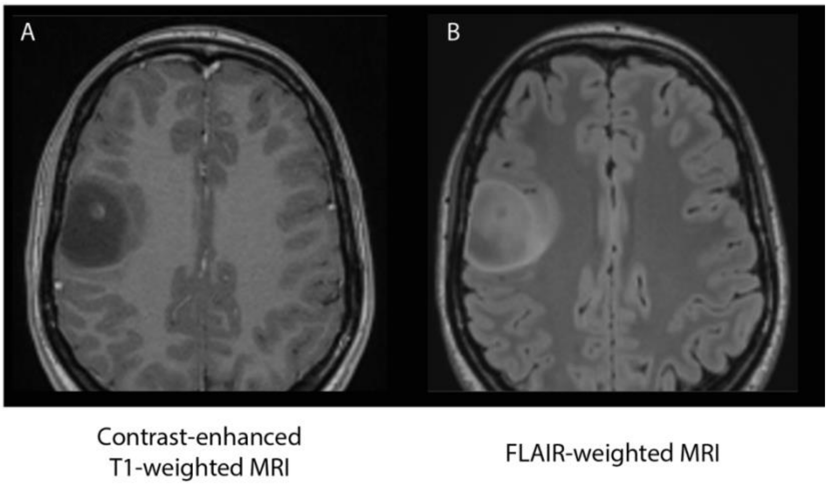

MRI from a patient with an IDH-mutant glioblastoma. A. Contrast-enhanced axial T1-weighted MRI with only little contrast enhancement. B. FLAIR-weighted axial MRI with complex signal intensity due to different T1-relaxation times. The images were taken at the Department of Neuroradiology from the Medical Centre – University of Freiburg.

1.2.2. Treatment and Outcome

Therapy strategies differ between low-grade and high-grade tumours for the reasons mentioned above. With that saying, in high-grade gliomas, a safe gross-total resection of the contrast-enhancing tumour followed by adjuvant radio-chemotherapy is the standard first-line treatment of choice[8,9]. However, in some patients where the tumour growth presents in eloquent and deep-seated areas, a biopsy instead of a resection can precede adjuvant treatment for histopathological and molecular diagnosis. Recent studies have suggested the possibility of introducing neo-adjuvant immunotherapies in high-grade gliomas, however the gold standard remains unchanged [10,11].Despite best available treatment the median overall survival rate is about 16 months [4,12].

In the case of low-grade gliomas, a standard treatment has not been established. This is due to the more heterogenic course of disease and a lack of consistent evidence compared to that in high-grade tumours. Nonetheless, it has been reported that attempting a maximum safe resection does have an impact on survival among these patients [13]. The timing of surgery, however, is still controversial as is the chemotherapeutic agent of choice, but the discovery of new mutations has opened the possibility of developing targeted therapies. Radiotherapy, in combination with chemotherapy, poses a survival benefit over radiotherapy alone [14]. Patients with low-grade gliomas have a more prolonged overall survival than those with high-grade gliomas, but the first still have a tendency towards malignant progression, for which the median overall survival lies at 5 to more than 15 years [15].

1.2.3 Classification

The World Health Organization published in 2016 a major revision of the Classification of Tumours of the Central Nervous System, which lead to more than one hundred official tumour entities. Pathologies that may have similar histological features are now more clearly differentiated from one another according to their molecular profile. This has shown to be extremely relevant not only for diagnosis, but also for prognosis in terms of response to adjuvant therapy and survival [16]. Tumours are classified according to their histological characteristics and genetic alterations as shown below:

Figure 7

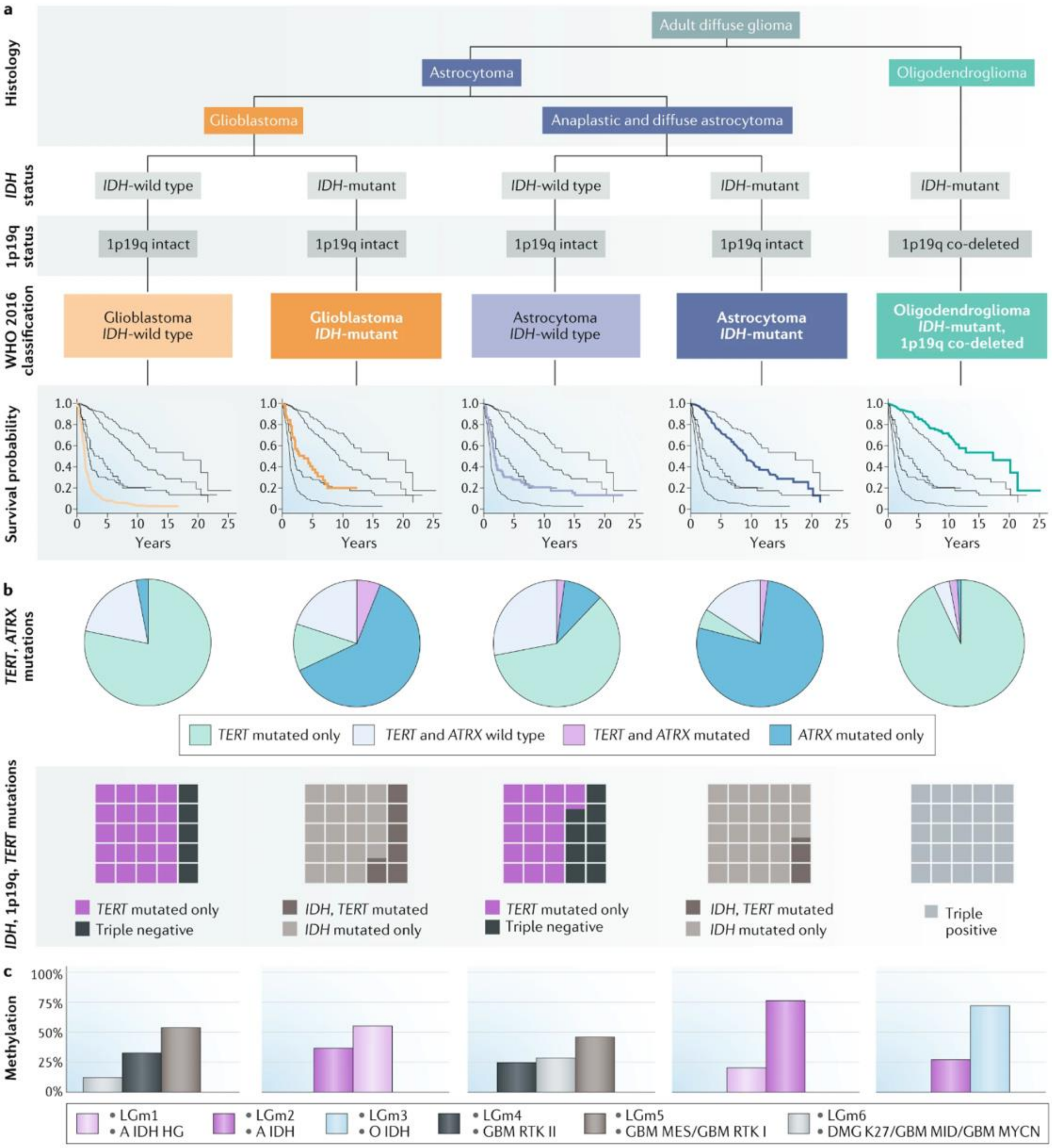

Diagram for diagnosis in gliomas. Taken from [17].

1.2.4. IDH Mutation

Since 2009, the mutation of isocitrate hydrogenase (IDH) 1/2 is known to have a relevant role in gliomas by inhibiting both histone and DNA methylation and disturbing epigenetic regulation. A tumour-derived mutation in the catalytic region of the IDH 1/2 gene produces the oncometabolite 2-hydroxyglutarate (2-HG) instead of α-ketoglutarate (α-KG), which leads to reshaping the epigenome, increasing the methylation of CIMP genes and thereby altering the epigenetic control of stem and progenitor cell differentiation [18].

Figure 8

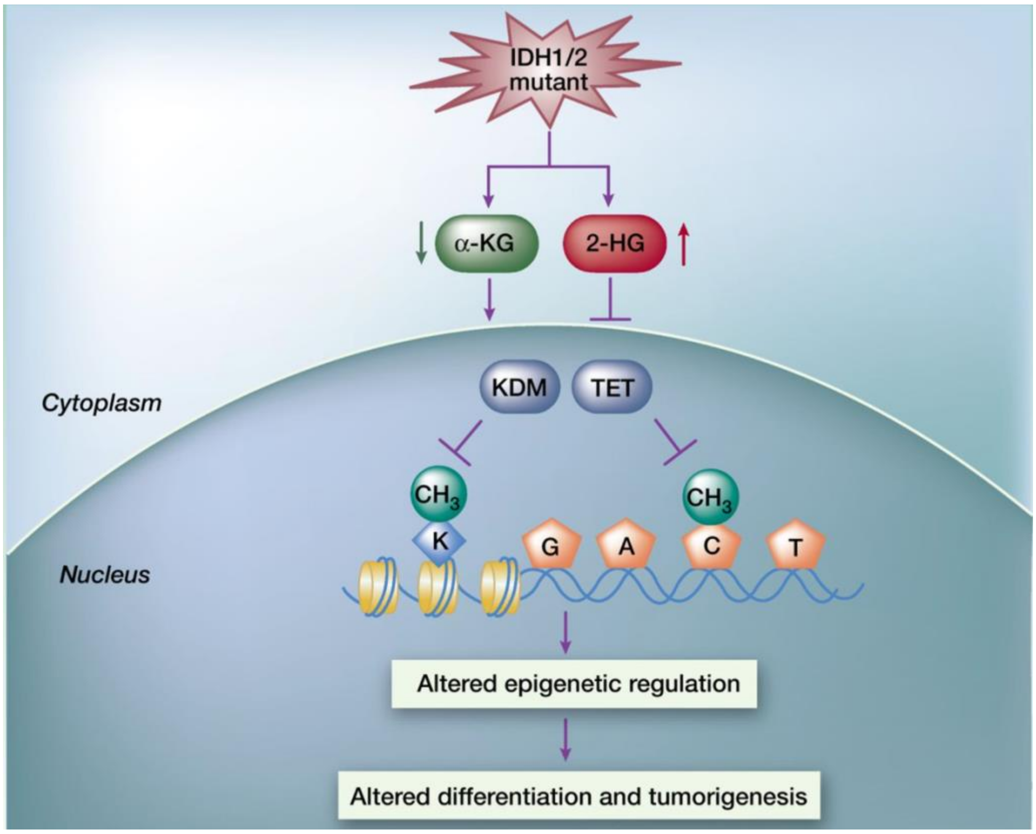

Effects of an IDH (1/2) mutation. Taken from [19].

Defining the presence or absence of an IDH (1/2) mutation is now necessary for the correct diagnosis in gliomas. Tumours with an IDH-mutation also present a TP53 mutation, ATRX loss, limited TERT promoter mutations, notable EGFR amplifications and PTEN mutations and are further divided according to histology into either diffuse astrocytoma, anaplastic astrocytoma or glioblastoma (IDH-mutated) [4,20]. Gliomas with an IDH-mutation and a loss of heterozygosity due to the combined deletion of 1p/19q are oligodendrogliomas (either sole oligodendroglioma or anaplastic, depending on histology). Gliomas without an IDH-mutation are IDH-wildtype glioblastomas and characteristically present gains in chromosome 7 and losses on chromosomes 10 (most significantly) and 9 (less frequent) [4,21]. IDH-wildtype gliomas are clearly correlated with a worse clinical outcome and reduced treatment response.

1.2.5 Common molecular alterations

MGMT or O^6-methylguanine DNA methyltransferase is a nuclear enzyme that removes alkyl groups from the O^6-position of O^6-MG, a task which is directly affected by the abundance of the MGMT enzyme. In the case of low MGMT expression and therefore failed repair of O^6-MG, the cell repair cycles cannot be completed, leading to cell cycle arrest and cell death. In the case of a promotor methylation of MGMT, MGMT expression is reduced, thus making the effects of an alkylating chemotherapy such as temozolomide significantly greater by avoiding the DNA repairing activity. Patients with this methylation show a better response to chemotherapy and combined adjuvant treatment on the hole [22].

Gliomas with a K27M mutation in the histone H3 gene H3F3A or the HIST1H3B genes that present a diffuse growth pattern arising from brain structures in a midline location, such as the thalamus or brain stem, are now defined as diffuse midline gliomas, H3 K27M-mutant. The discovery of this mutation has helped to pave the way for the development of directed tumour therapies [4,5].

BRAF V600, a mutation that has been found in other cancers such as melanoma and non-small cell lung cancer, has also been found in different gliomas, most frequently in pleomorphic xantoastrocytomas and gangliogliomas (70-80%) and less frequently in high-grade gliomas (3%) [16,23,24]. This mutation is also on the spotlight for targeted therapy research.

Many other mutations are being researched and have been described in other brain tumours besides gliomas (i.e., medulloblastoma) with the purpose of better characterizing brain tumours, however their mention is beyond the scope of this research.

1.3. Magnetic Resonance Spectroscopy

Magnetic resonance spectroscopy (MRS) determines the metabolic state of a brain lesion. In ^{1}H MRS, MR spectra are recorded from protons (^{1}H) attached to other molecules, as the former are highly sensitive and biologically abundant in the central nervous system. MR spectroscopy can be performed from one determined region of the brain, as in single-voxel spectroscopy, or from various regions, as in chemical-shift-imaging [25–28]. The resulting MR spectrum comprises resonances or peaks from different metabolites expressed in parts per million, or ppm, a radiofrequency scale. The metabolites in the 1-5 ppm range are the ones analysed in the clinical setting (in-vivo ^{1}H MRS) [26,29–31] .

1.3.1 Brain metabolites detected by MRS

N-acetyl aspartate (tNAA, from NAA + *N*-acetylaspartylglutamate)) is a neural metabolite, it is synthesized in the mitochondria of neurons, and then transported along the cytoplasm to the axons. This metabolite is present solely in the central and peripheral nervous system and thus is the marker for normal brain as an interpretation of the viability of the neural structures. Researchers have also found this metabolite in oligodendroglial and astrocytic progenitor cells, but it is clearly absent from extra-axial lesions, such as meningiomas. tNAA has the highest peak in normal brain at 2.02 ppm [26,32].

Creatine (tCr, from Cr and phosphocreatine), which resonates at 3.0 ppm, marks active intracellular metabolism (for example from brain and heart-muscle tissue) and is a relatively stable metabolite, albeit regional (more concentration in grey matter) and individual variabilities. tCr is more often increased in gliosis, which sometimes aids in the differentiation between gliomas and brain metastasis [26,33].

Choline (tCho, from choline, phospho-choline + glycerophosphocholine), resonates at 3.22 ppm. This metabolite is a precursor of acetylcholine (ACH), which is a component of the cell membrane. Pathologies with a high cellular membrane turnover, such as neoplasms, demyelination, infarction, inflammation and glial proliferation, show higher concentrations of tCho, whereas necrotic areas show low or absent concentrations. tCho is usually clinically relevant when compared to tNAA and tCr concentrations (tCho/tNAA and tCho/tCr ratios) [26,27,32].

Inositol (mIns) resonates at 3.55 ppm, is a precursor of phosphatidylinositol and phosphatidylinositol 4,5-bisphosphate, is involved in cell signalling transduction and it is supposed to be a product of myelin degradation. It has been described as the most important osmolyte in astrocytes and is present in inflammation and proliferating glial cells. Various pathologies such as low-grade astrocytoma and progressive multifocal leukoencephalopathy show increased concentrations of this metabolite, while malignant tumours such as glioblastoma show decreased or absent signals. It has also been suggested that this metabolite can be used as a marker for monitoring hepatic leukoencephalopathy and hyponatraemic brain disorders [26,33–36].

Figure 9

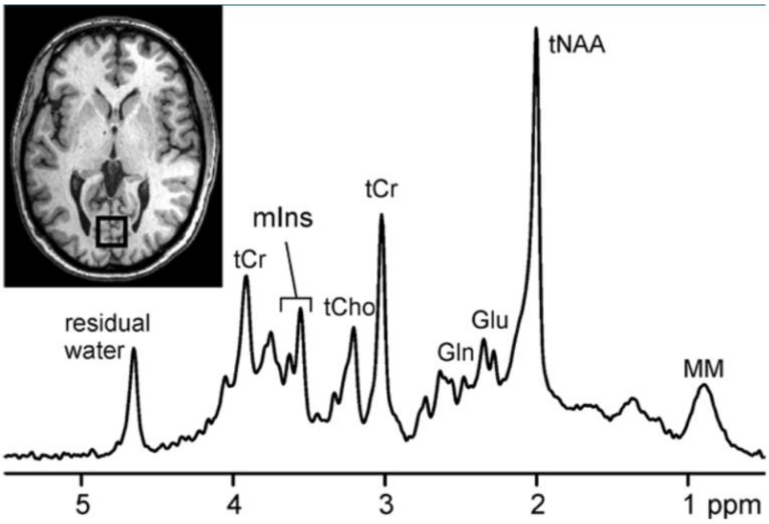

^{1}H MR spectrum (3.0 T, VOI 20 x 20 x 20 mm^3) from the occipital lobe of a healthy participant. Taken from [32].

Glutamate and Glutamine (Glu and Gln respectively or Glx as the sum of both) have peak complexes at 2.2-2.50 ppm, but often the complex overlaps the γ-aminobutyric acid (GABA) peak, which is why at least a 3T MR scanner is necessary to visualize the separated peaks. Glu is a very important excitatory neurotransmitter and both metabolites are key elements of the Krebs cycle and mitochondrial redox systems, making them markers of metabolic brain disorders, stroke and other associated lesions [33,34,37].

Alanine (Ala) resonates with a doublet peak at 1.48 ppm and has been shown to be elevated in meningiomas [26].

Lipids resonate at 1.2 ppm (methylene group of fatty acid) and at 0.9 ppm (methyl group of fatty acid), are visualized with short echo times (TE) (because of their short relaxation time) and are not usually visible in normal brain. As lipids are integral elements of the cell membranes, the peaks are seen in situations of cellular membrane disruption as in the presence of abscesses, malignant primary tumours, metastasis and necrosis, where there is also an overlap with the peak of macromolecules (broken-down proteins) [26,32,33].

Lactate resonates at 1.3 ppm and is visualized as a doublet at long echo times, inverted in intermediate echo times and merged with lipids at short echo times. Lactate is a product of anaerobic glycolysis secondary to anaerobic metabolism and is therefore not found in the normal brain. Triggers of anaerobic metabolism are cerebral hypoxia, ischemia, seizure, mitochondrial metabolic disorders, inflammation, some cysts and necrosis [25–27,32,33].

Figure 10

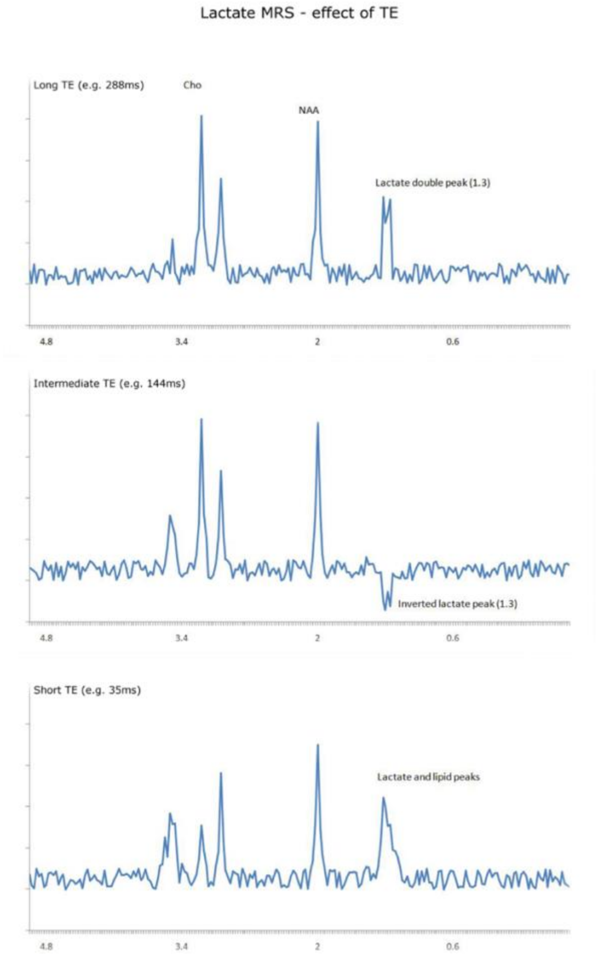

Sample spectra of the effect of TE on lactate signal. Image courtesy of Assoc. Prof. F. Gallard, Radiopedia.ord, rID: 36021

1.3.2 Prediction of genomic features with MRS

The technical advances in magnetic resonance scanners have allowed for more precise and sensitive data acquisition through magnetic resonance spectroscopy [38,39]. Consecutively, MRS has evolved from a tool able to examine the metabolic and functional alterations of brain lesions to also correlating and uncovering the molecular mechanisms behind these.

Since the 1990s, studies on patients with brain lesions and primary brain tumours have shown that MRS can distinguish between different grades of malignancy and even intratumoral heterogeneity [30]. As mentioned before, peaks or absences from certain metabolites can discriminate between different brain lesions [26,32–34,40]. Based on these principles, metabolite ratios have been studied extensively in order to establish schemes that can aid radiologists and clinicians alike in the interpretation of MRS results [41,42]. In paediatric cerebellar tumours, a multicentre study has validated the importance of adding MRS to the routine MRI diagnostic workup and showed the prognostic value of the biomarkers identified through imaging and also developed an automated tool implemented in the automatic analysis of peak metabolite ratios and the classification of different pathologies [42–44].

In gliomas, Choi et al. described in 2012 the detection of 2-HG concentrations, the oncometabolite generated by the IDH 1/2 mutation by means of MRS [45]. Further studies confirmed that 2-HG has a positive peak at 2.25 ppm in tumour tissue and is absent in normal brain. This enables not only to diagnose and classify tumours but is also a non-invasive way to monitor patients and treatment response. However, the concentration of this oncometabolite is particularly dependent on tumour volume, which lowers the sensitivity of MRS in small tumours [45,46].

Figure 11

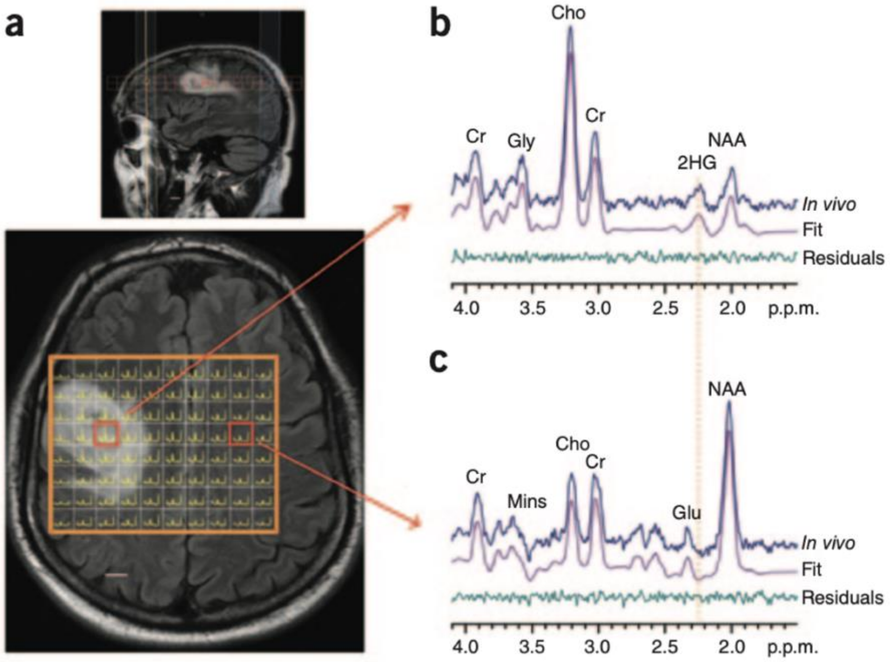

a) CSI imaging of a patient with an oligodendroglioma WHOºIII overlaid over a FLAIR sequence. b) Representative spectrum from the tumours showing 2HG resonating between 2.2 and 2.3 ppm. c) NAA concentration confirms the contralateral normal brain. Taken from [45].

Following these investigations, a study by Heiland et. al showed the successful correlation between metabolites and the genetic alterations and molecular pathways of glioblastoma [47]. Then, Diamandis et. al. described a machine learning model able to predict the molecular subtype of gliomas based on MRS [48].

1.4. Objective

The importance of developing automated analysis tools lies in the possibility of a straightforward application and simplified interpretation of CSI and genetic data that allow for incorporation into the daily practice of a broad audience. The purpose of this study is:

1. The development of a straightforward tool that can easily be used to preoperatively predict and correlate the metabolic signature of different CNS-lesions.

2. Integrating the molecular profile of gliomas into the prediction model.

3. Delivering an open-software tool with the possibility of advancing the diagnostic work-up of gliomas to the latest standards.

2. Materials and Methods

2.1. Study Design

The present study is a prospective, single centre, single arm, diagnostic study trial started in 2016. It is being conducted at the Departments of Neurosurgery and Neuroradiology of the Medical Centre of the University Freiburg, has been approved by the Ethics Committee of the Medical Centre of the University Freiburg (protocol 360/16_170908) and registered at the German Clinical Trials Register (DRKS) under DRKS00019855.

2.2. Patient Enrolment

Patients undergoing diagnostics and treatment for high- and low-grade brain lesions were enrolled in the study. Participants were deemed eligible for the study if they matched the following inclusion criteria: 1) brain lesion not located near the skull base, 2) no contraindication for undergoing MRI, 3) no contrast-enhancement allergy. All subjects signed a written informed consent for participation in the study and a personal data protection clause according to German and European Standards for Data Protection.

Following the informed consent, patients received preoperative anatomical and in-vivo chemical shift imaging (MR-spectroscopy) and underwent either biopsy or surgical resection for their respective lesions after previous discussion of the case by our centre’s multidisciplinary tumour board. Patients with a suspected tumorous lesion without definite histological diagnosis were excluded from further analysis. In case of an inflammatory lesion (i.e., encephalomyelitis) or haemorrhage, a histological diagnosis was deemed unnecessary if the patients met the respective radiological and clinical criteria for a diagnosis (e. g. MS and encephalomyelitis).

2.3. Imaging Acquisition and Data

Preoperative anatomical and in-vivo chemical shift imaging were performed at a whole-body system 3T MR Magnetom Prisma scanner (Siemens, Erlangen, Germany) in the Department of Neuroradiology, Medical Centre - University Freiburg. Anatomical imaging included a 3D SPACE Dark Fluid sequence (TR= 5000 ms, TI= 1800 ms, TE =388 ms, echo train length 251, voxel size 1 mm^3), a 2D T_2 weighted turbo spin-echo sequence (TR= 4500 ms, TE= 100 ms, echo train length 17, voxel size 0.6 × 0.6 × 2 mm^3) in the geometry of the CSI - sequence, and a 3D T_1-weighted sequences (MPRage, TR= 2300 ms, TI= 988 ms, TE= 2.26 ms, voxel size 1 mm^3) before and after application of 0.1 mM Gadoteridol per kg body weight [ProHance®, Bracco, Konstanz, Germany]. Spectroscopic imaging was performed using the manufacturer's provided 2D chemical shift imaging (CSI) sLASER sequence with a TR = 1500 ms, TE =40 ms (5 x 5 x 20 mm^3 voxel size), Table 1**.**

Figure 12

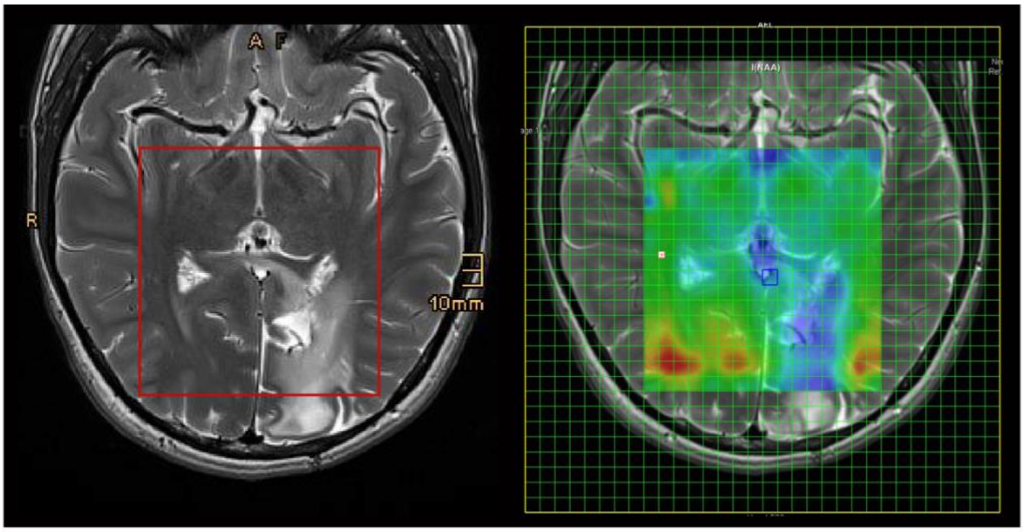

ROI definition on MRI

MRS

Example of ROI generation of an IDH wildtype glioblastoma on a T2-weighted MRI.

Table 1

Mode	Duration (in minutes)
Preparation of the patient	05:00
FLAIR 3D	07:52
T2-high resolution TSE	02:38
CSI-slaser, TE 40 ms (VOI: 5 x 5 x 15 mm^3)	20:12
T1-MPRage post-contrast	03:54
Total	38:56

Measurement times of the preoperative anatomical and in-vivo chemical-shift imaging.

2.4. CSI Processing

Raw spectra were downloaded in the RDA file format (Siemens, Erlangen, Germany) and loaded into "R" using the package "spant". The data were analysed by an internal pipeline including baseline correction and fitting using Totally Automatic Robust Quantitation in NMR (TARQUIN). TARQUIN is a free software that can automatically quantify the measured concentrations of metabolites in the spectra. The pipeline required the following input parameters: A folder containing all input files, a vector with all unique identifiers of each patient or RDA file (we used a random patient's ID for the filename, e.g., 123.RDA) and an output folder. The "SPORT_Basic.R" file is available at: github.com/heilandd/SPORT/R. After a successful pipeline run, the output folder contained all RDS files with a list of the baseline fitted spectra, the fitted metabolites and the annotation data (which at this point haven't been defined). Then the anatomical annotations (segmentation) were defined using a shiny toolbox.

2.5. Segmentation

For segmentation of each voxel, an interactive web application software tool "shiny" from R Studio was developed in collaboration with The Milo Lab. This tool is available online and can be accessed everywhere (https://nchneuro.shinyapps.io/radweb/

Username/password: “test”). The output RDS files which were generated after the CSI processing and an anatomical reference are uploaded into the previously mentioned shiny tool app.

Figure 13

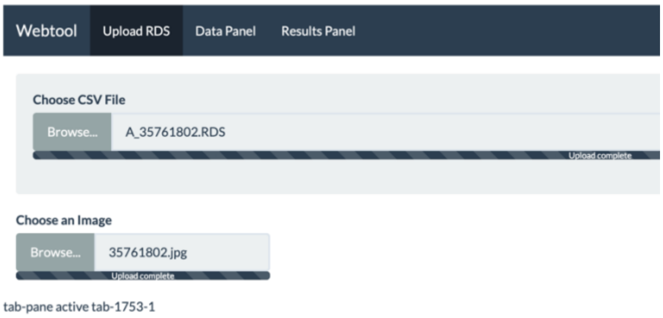

Choose CSV File
A_35761802.RDS
Upload complete

Choose an Image
35761802.jpg
Upload complete

tab-pane active tab-1753-1

Snapshot of the homepage of the shiny app, where the files can be uploaded.

The RDS files (in the app labelled “CSV-file”) and the MRS files (in the app labelled “Image”, as they are uploaded as .jpg files) were uploaded to the app. The anatomical image is aligned to the reference given by a 32x32 voxel raster. The alignment can be done by fitting the image into the given raster (by changing the x and y scale). The MRS grid was then aligned to the FLAIR-, T2- and contrast-enhanced T1-weighted images.

Figure 14

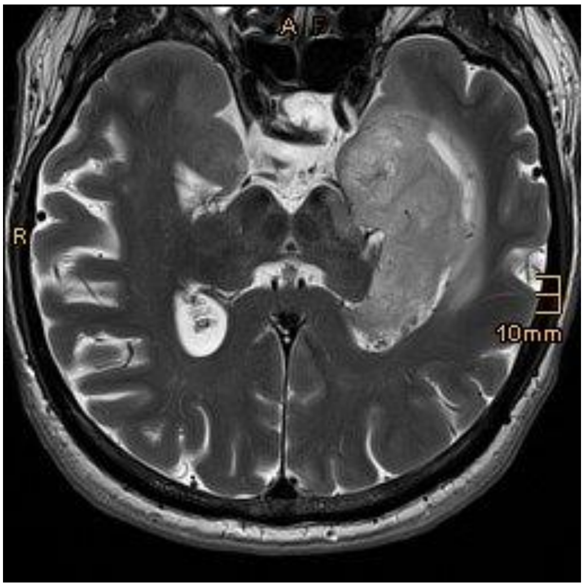

Anatomical reference showing the left temporal tumour mass on a T2-weighted MRI sequence.

Figure 15

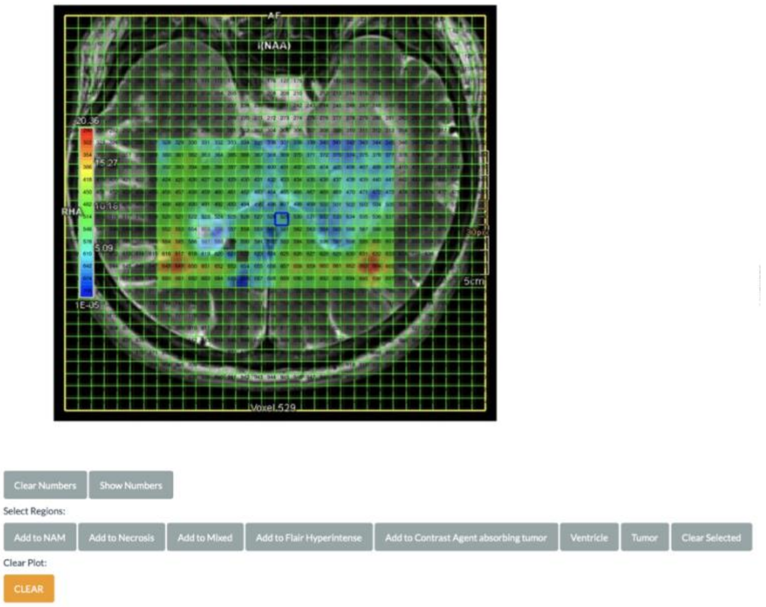

Screenshot of the shiny segmentation app with the aligned MRS. On the left, x- and y-axis can be adjusted for the alignment of raster and anatomical image, as well as the angle.

Figure 16

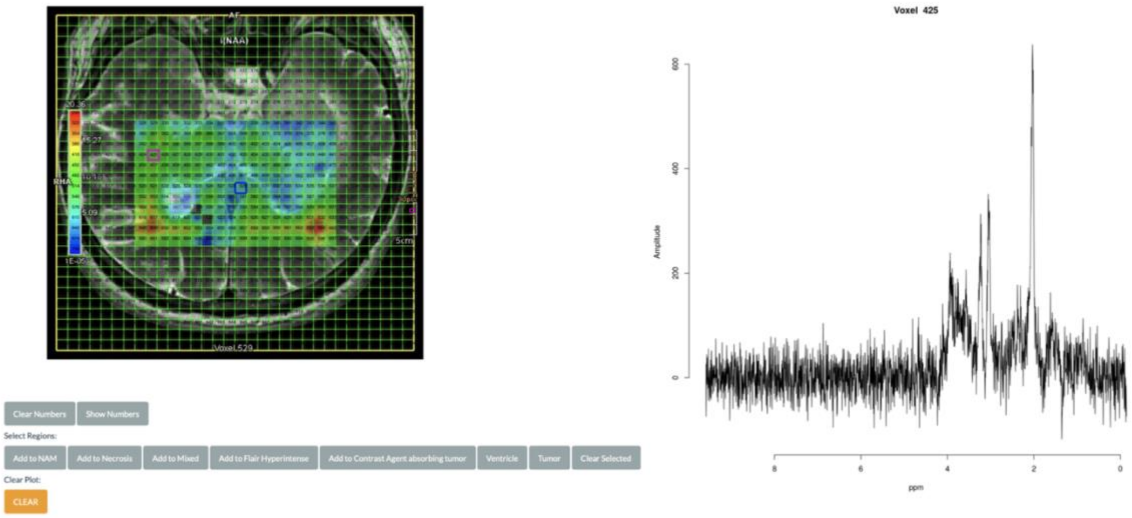

Raw spectrum depicting Voxel “425” (in purple), which was aligned to normal-appearing matter (NAM), because of the characteristic highest peak at around 2.02 ppm of NAA.

Each spectrum (raw data) can be accessed by double-clicking on the voxel. For the semi-automatic segmentation, the voxels can be marked by clicking and dragging a selection box in the voxel of interest and adding the tag (e.g., NAM) of interest to the selected voxels.

The regions were assigned as follows: normal appearing matter (NAM), mixed (i.e., tumour and ventricle), lesion (i.e., ischemia, inflammation), tumour, contrast-enhancement, necrosis, FLAIR hyperintense regions or ventricle system. Each spectrum was supervised and excluded if quality criteria based on fitted residuals was not achieved. Segmentation and raw files were then downloaded for further analysis.

Figure 17

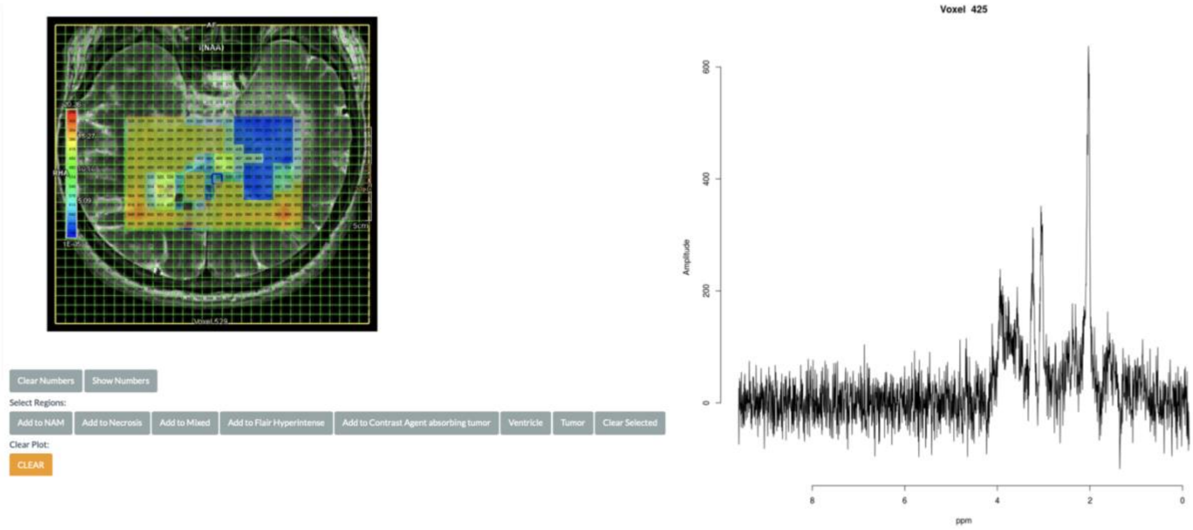

Snapshot of the shiny segmentation app, colours depict the segmented regions.

2.6. Tumour Tissue Sampling

Navigation-based tissue sampling (Cranial Map Neuronavigation Cart 2, Stryker®, Michigan, United Stated of America) was performed after previous planning by the surgical team at the Department of Neurosurgery of the Medical Centre - University Freiburg. Sampling locations were aligned to the MR spectroscopy voxels by integration into the neuronavigation system. In high-grade glioma, sampling was taken from the contrast-enhancing regions and in low-grade lesions from the T2-hyperintense regions. Tissue samples were immediately snap-frozen in liquid nitrogen and processed. Histopathological diagnosis was performed at the Institute of Neuropathology, Medical Centre - University Freiburg according to their standards, including IDH immunohistochemistry and genome analysis (1p19q co-deletion (LOH) and exome sequencing of IDH1/2).

2.7. Deep Autoencoder for Denoising

Data denoising was done in collaboration with the Milo Lab. First, for estimating a gaussian distribution conditioned on the input matrix containing 34 metabolites (which is the standard metabolite output of TARQUIN), an autoencoder framework was applied. For the input layer, the metabolites were normalized and scaled:

$$(1) norm(x) = \frac{x - min(x)}{max(x) - min(x)}$$

An autoencoder consists of two parts: an encoder and a decoder, which can be defined as transitions:

$$(2) encoder: \phi: \mathcal{X} \rightarrow \mathcal{F} decoder: \psi: \mathcal{F} \rightarrow \mathcal{X}$$

A sigmoid activation function with a minimal dropout (b=0.1) was recently described as being beneficial for precise data reconstruction and denoising [49]. The activation function was defined as follows:

$$(3) \sigma(x) = \frac{1}{1 + e^{-x}}$$

The encoder stage of an autoencoder takes the input $x \in \mathbb{R}^d = \mathcal{X}$ and maps it to $z \in \mathbb{R}^p = \mathcal{F}$ at the layer position φ :

$$(4) x = A^{\varphi=0}; z^{\varphi} = \sigma(W^{\varphi} \times A^{\varphi-1} + b^{\varphi})$$

z^{φ} is also referred to as *latent representation*, here presented as $z^1, z^2, \dots, z^{\varphi=n}$ in which φ describes the number of hidden layers. *W* is the weight matrix, and *b* represents the dropout or bias vector. The network architecture contained three hidden layers including a batch normalization with decreasing number of neurons (32,16, 8), followed by six bottleneck layers of neurons (Figure 8 and Figure 9) and the decoder part with mirrored composition. In the decoder, weights and biases are reconstructed through backpropagation ($\psi: \mathcal{F} \to \mathcal{X}$) and z is mapped as $x' = A^{0'}$ in the shape as x.

$$(5) A^{\varphi-1'} = \sigma'(W^{\varphi'} \times z^{\varphi} + b^{\varphi'})$$

In this setting, $W^{'}, \sigma^{'}, b'$ from the decoder are unrelated to W, σ, b from the encoder. Then, a loss function was used to train the network in order to minimize reconstruction errors.

$$(6) \mathcal{L}(x, x') = \left\| x - \sigma'(W'(\sigma(Wx + b)) + b') \right\|^2$$

Figure 18

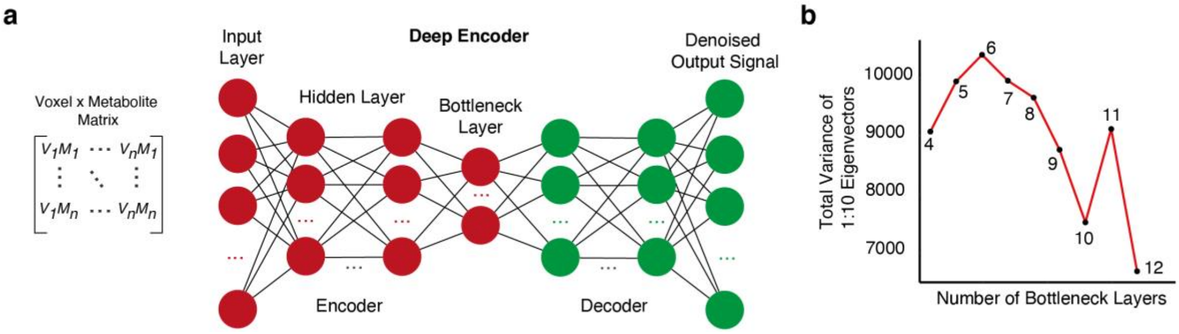

a) Working matrix and illustration of the neuronal network architecture. b) Hyperparameter tuning with a line plot of the total variance (first 10 components estimated by PCA) using different numbers of bottleneck layers (4:12). The maximal variance is shown to have been predicted at 6 bottleneck layers.

Figure 19

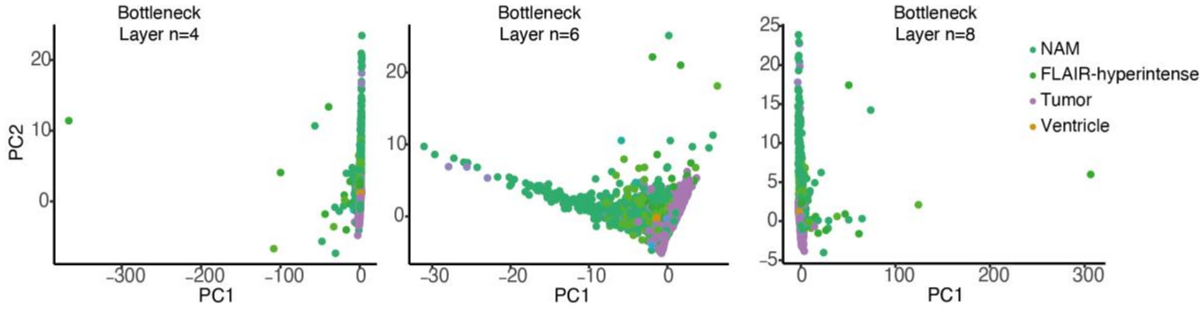

Scatterplots representing PC1 vs. PC2 showing the highest variance at six bottleneck layers.

2.8. Hyperparameter Search

For the purpose of defining the optimal number of bottleneck and dropout values, a network with an increasing number of bottleneck layers (n=4:10) was trained and the variance of the two first eigenvectors was determined as a benchmark to establish the maximum effectiveness of the denoising algorithm.

2.9. Prediction Model

A linear discriminant analysis (LDA) was used for prediction of the voxel origin (normal appearing matter vs. lesion) and the tumour subclass. LDA postulates that the conditional probability density functions are normally distributed (our denoised output (deep autoencoder) is normally distributed) when considering both mean and covariance parameters. The metabolic training data was defined as a set of observations $\underset{x}{\rightarrow}$ for each voxel with the known class μ. The input was defined as:

$$(7) x' = \sigma'(W^{\varphi'} \times z^{\varphi} + b^{\varphi'}) \sim \mathcal{N}(\mu, \sigma^2)$$

x' is the reconstructed vector x using the autoencoder. In addition, a simplifying homoscedasticity assumption that the covariances have full rank due to the deep autoencoder outputs was made. Here, a multiclass LDA was applied:

$$(8)\quad S = \frac{\underset{w}{\to}^{T}\times\Sigma_{b}\underset{w}{\to}}{\underset{w}{\to}^{T}\times\Sigma\underset{w}{\to}}$$

$$(9)\quad \Sigma_{b} = \frac{1}{C}\Sigma_{i=1}^{C}(\mu_{i}-\mu)(\mu_{i}-\mu)^{T}$$

in which $\underset{w}{\to}$ is the eigenvector and C represents the classes ($C=C_{NAM}, C_{T}, C_{L}$), and for the tumour classification: $C=C_{wt}, C_{IDH}, C_{LOH}$. The final classification score (SPORT classifier) is the mean of the estimated class predictors (LDA) resulting in a score for each determined class:

$$(10) s_{c(n)} = mean(\sum_{i}^{C} S(c))$$

2.10. Dimensional Reduction and Clustering

The eigenvalue frequencies of the first 30 principal components were decomposed and the number of non-trivial components was determined by comparison to a matrix containing randomized intensity values. The obtained non-trivial components were used for shared nearest neighbour (SNN) clustering followed by dimensional reduction using the Uniform Manifold Approximation and Projection (UMAP) algorithm. All steps were implemented in the previously mentioned software package in R developed by the Milo Lab.

Figure 20

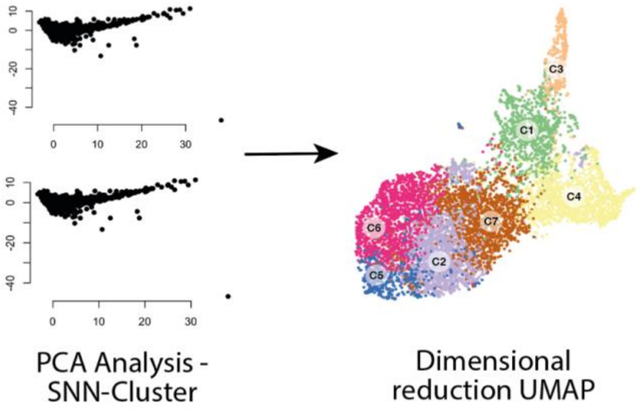

Example of PCA-Analysis-SNN-Cluster and consequent Dimensional reduction UMAP illustrating the SNN clusters.

2.11. Spatial Data Analysis

For the analysis of the spatial distribution, the SPATA [50] toolbox (spatial transcriptomic analysis) developed by the Milo Lab was optimized by using an MRS input function to create a “spata” S4 object. SPATA allows for determination of marker metabolites in space, trajectory analysis and metabolic architecture.

2.12. Mean Spectra

All presented mean spectra were estimated by the mean and variance of the baseline corrected raw spectra. Spectra were plotted by the ppm (x-axis) and the intensity (y-axis). The plotted lines indicated the mean signal intensity. The spectra were heat-coloured representing the regions of most variance using the inferno colour scheme (details in “Results” section).

3. Results

3.1. Patient demographics

The enrolment of patients in this prospective imaging trial started in August of 2016 and, until October of 2019, 120 patients were enrolled. From this set of patients, deviations from the study protocol were detected in 23 patients, including erroneous MRS parameters (n=8), bad shimming (n=2) and wrong voxel size (n=13). Additionally, six patients whose diagnosis was either clinically and/or histologically uncertain or who were lost to follow-up after imaging were excluded from further analysis. 91 datasets from 90 patients (one patient was imaged at diagnosis and first recurrence) were suitable for further analysis. The most frequent localization of a lesion was the frontal lobe (34 patients, 37,7%), followed by the temporal (22 patients, 24,4%), parietal (17 patients, 18,9%) and occipital (8 patients, 8,9%) lobes. Other localizations are shown in Figure 11.

Table 2

Characteristic	**N=90**	**%**
Gender		
Female	38	42,2
Male	53	58,9
Age (years)		
Median	52,6	
Range	(16-84)	

Demographic characteristics of the patient population included in this study.

Figure 21

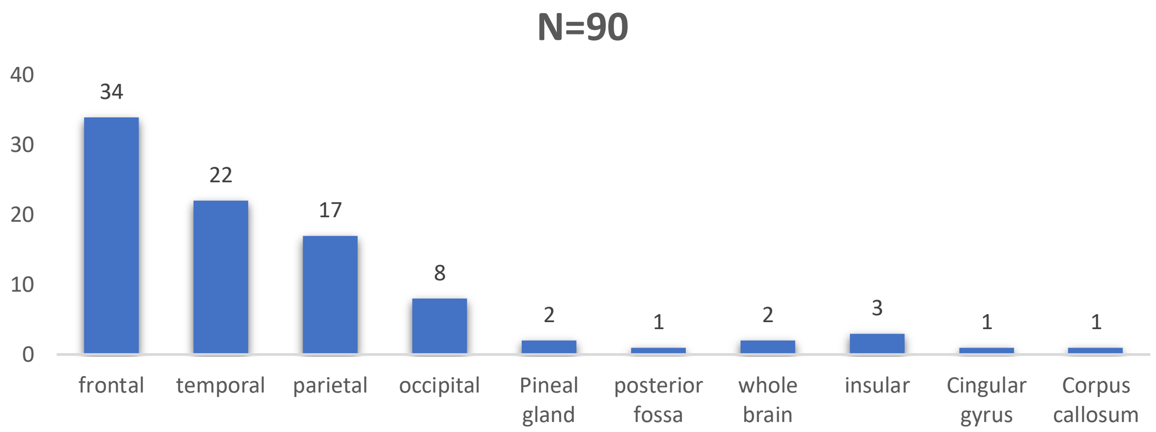

Bar plot of frequency distribution of anatomical localization of brain lesions included in the study.

Gliomas were the most frequent pathology representing 73% (n=65) of all patients. Within gliomas, those with a wildtype IDH-status were more common (n=35, 53,8%, histopathologically defined glioblastomas, WHO grade IV), followed by those with a mutated IDH-status (n=17, 26,2%, histopathologically defined as diffuse and anaplastic astrocytoma, WHO grades II and III respectively) and lastly there were n=13 patients with a mutated IDH-status combined with a codeletion of 1p/19q (LOH, 20%, histopathologically defined as oligodendrogliomas WHO grades II and III).

Figure 22

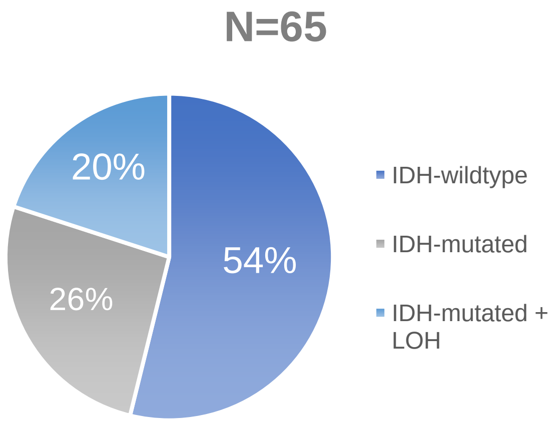

Frequency distribution of gliomas according to IDH (1/2) mutation included in the study.

Figure 23

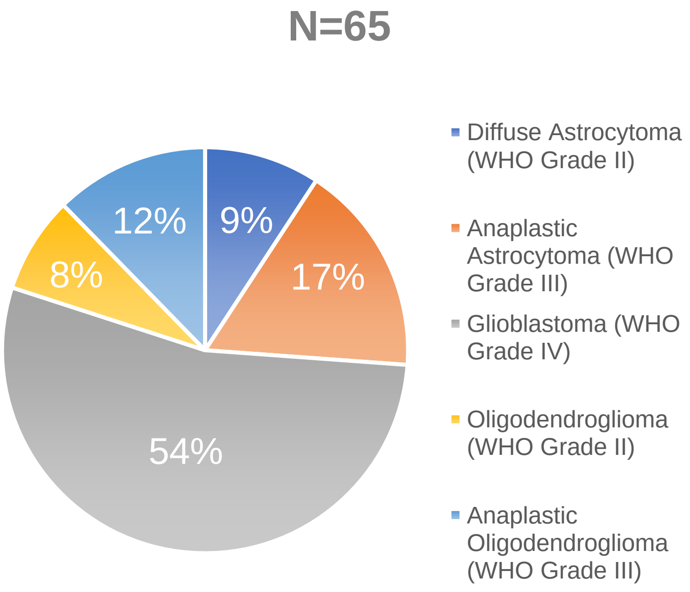

Frequency distribution of gliomas according to histology included in the study.

A broad spectrum of different pathologies was also present in the study (Figure 24), such as dysembrioplastic neuroepithelial tumours (DNET), ependymoma, pineal gland tumours, metastatic lesions from melanoma and non-small-cell lung carcinoma (NSCLC) and focal cortical dysplasia (FCD).

Figure 24

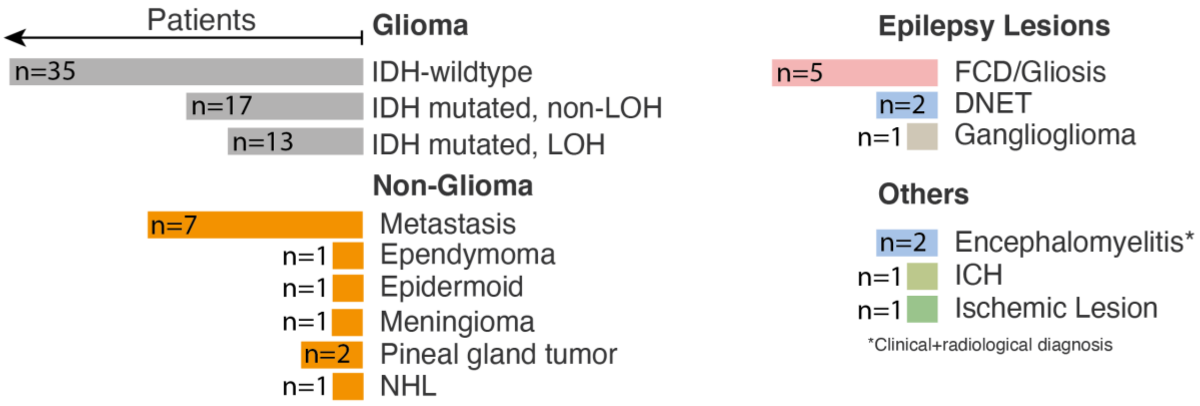

Frequency of pathologies included in the study.

3.2. Unsupervised analysis of metabolomic heterogeneity and diversity in MRS data

A pipeline for unsupervised analysis using computational approaches predominantly applied to high-dimensional data analysis was used in order to gain insights into the diversity and spatial distribution of 22.438 spectra (obtained from 91 ^{1}H MRS studies). After the MRS data acquisition, metabolites of each voxel using Totally Automatic Robust Quantitation in NMR (TARQUIN) were fitted followed by the segmentation of each voxel into normal appearing matter (NAM), ventricle, mixed, FLAIR-hyperintense region, non-contrast enhancing tumour and contrast enhancing tumour. Voxels that couldn't be allocated in a straightforward matter or contained overlapping regions were excluded from the initial data analysis to ensure that the training data set was as accurate as possible. Data denoising was performed using a deep autoencoder with six bottleneck layers (as previously mentioned in the "Methods" section), which revealed an improved data quality. A hyperparameter optimization was used to estimate the dropout in the hidden layers and the optimal number of bottleneck layers was established. After denoising, a principal component analysis (PCA) was done, and non-trivial eigenvectors with higher eigenvalues compared to a PCA of randomized metabolic intensities (details in the "Methods" section) were selected.

The first twelve components were used for Uniform Manifold Approximation and Projection (UMAP), a previously mentioned method for dimensional reduction. Then, a shared-nearest-neighbour clustering was carried out, by which ten different clusters and the marker metabolites of each cluster were identified.

3.3. Cluster analysis reflects regional differences and pathological spectra

In the cluster analysis, clusters 1,2,4,5 & 7 revealed high intensities of N-acetyl-aspartate (NAA) and creatine (Cr), suggesting that this clusters predominantly contain normal appearing matter. Most of these voxels were also segmented as normal appearing matter, which confirmed our MRS data. The computation of sum spectrum of all voxels in those clusters showed a normal configuration. The intensity of NAA was found to be the most variable parameter. All other clusters revealed an altered pattern with various metabolic disbalances.

Figure 25

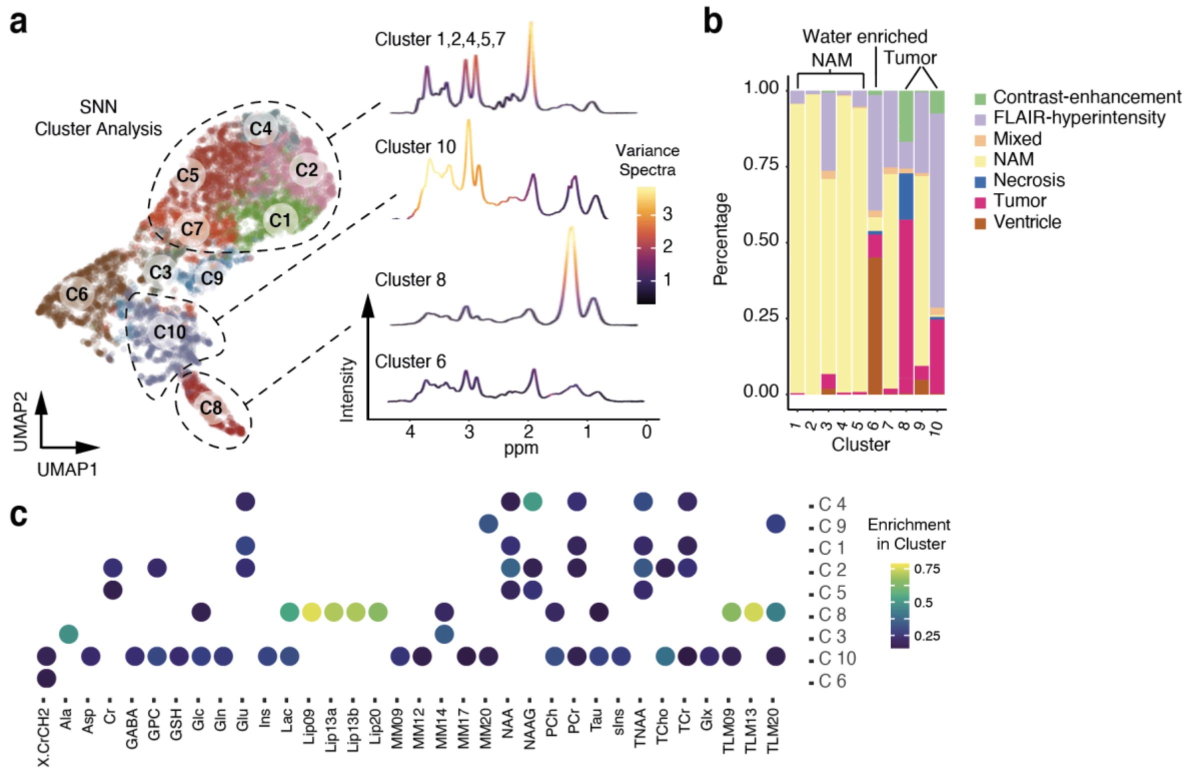

a) 2D representation of a UMAP dimensional reduction. Colours illustrate the SNN clusters (1-10). b) Bar plot indicates the distribution of the segmented voxels within the cluster analysis. c) Dot plot of significantly enriched metabolites of each cluster. Colours indicate the global intensity of each metabolite.

In cluster 8, the metabolic pattern was dominated by lactate and increased macromolecules. This cluster contained voxels of the contrast-enhancement regions as well as necrotic tumour regions. The spectra showed high intensities at 1.3 ppm (lactate) and between 1-0.6 ppm (MM and lipids), which is characteristic of malignancy.

Figure 26

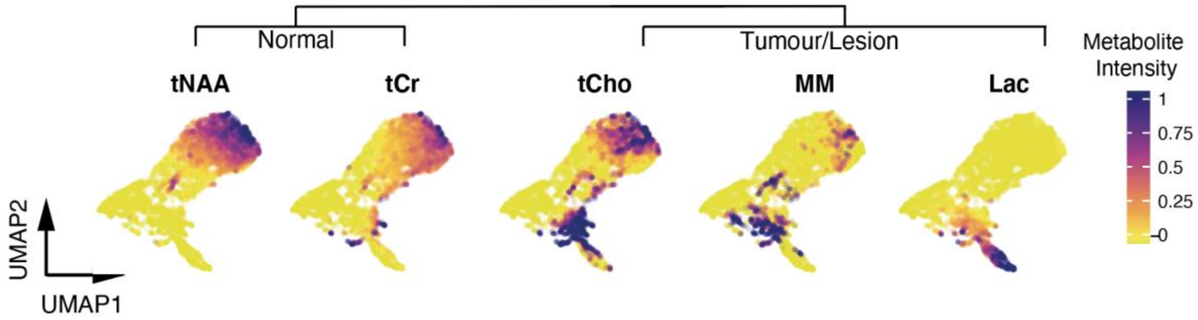

2D representation of a UMAP dimensional reduction. Colours illustrate the metabolite intensity and marker metabolites of each cluster region.

The next relative distant cluster 6 contained all ventricular segmented voxels and was marked by voxels with low or absent signal intensity. Additionally, it was found that voxels, which were segmented as FLAIR hyperintensity, were also enriched in this cluster. This leads to the assumption that the voxels of FLAIR-hyperintense regions of clusters 3,9 and 10 significantly differ to the FLAIR-hyperintense voxels of cluster 6. Clusters 3 and 9 lack classical tumour-related metabolites, such as those present in cluster 8, suggesting that the FLAIR-hyperintensity within the voxels is most probably due to vasogenic oedema rather than infiltrating high-grade tumour regions.

Figure 27

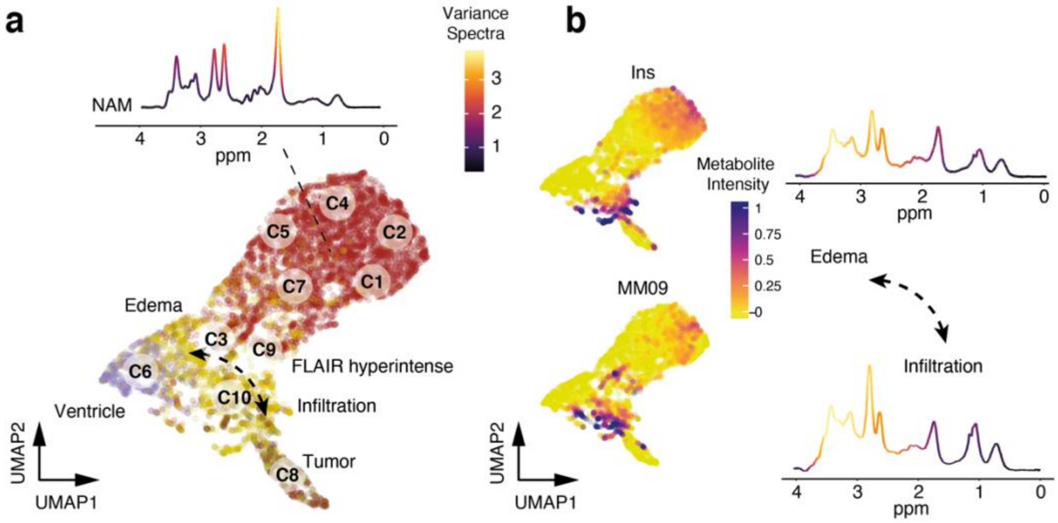

a) 2D representation of a UMAP dimensional reduction. Colours illustrate the regions, red: normal-appearing matter (NAM), yellow: FLAIR-hyperintensity, brown: tumour, and purple: ventricle. FLAIR-hyperintensity regions are partly assigned to the ventricle regions (which contained a low signal) and the tumour clusters, illustrated by a double arrow. b) On the left: 2D representation of a UMAP dimensional reduction. Colours illustrate marker metabolites Inositol (Ins), highly enriched in a FLAIR hyperintense region corresponding to oedema and a macro-molecule band (09) highly enriched within tumour-infiltrative regions. On the right: Representative spectra of the FLAIR-hyperintensity oedema region (top spectra) and FLAIR-hyperintensity tumour infiltration-related voxels (bottom spectra).

3.4. Prediction of tumour regions

A neural network was trained with a subsequent linear discrimination model to predict the output variable: normal appearing matter, metastasis, glioma or inflammatory lesion. The model was trained based on the segmented voxel (approx. 2/3 training and 1/3 validation, n=~8.000); then the findings were externally validated at a spatial resolution within ~23.000 voxels from the whole dataset. A prediction score which was fitted by a probability distribution model was computed, centred and scaled. With an outcome of 97.3% probability of correctly classified voxels, the automated designation of pathological voxels is relatively robust. Prediction of the other subgroups revealed a lower accuracy for the whole model (83.43%). A spatial grid of MRS was used for tumour prediction with which the tumour extension on the MRI could be reconstructed. In summary, normal and pathological MRS data can be distinguished with high accuracy.

Figure 28

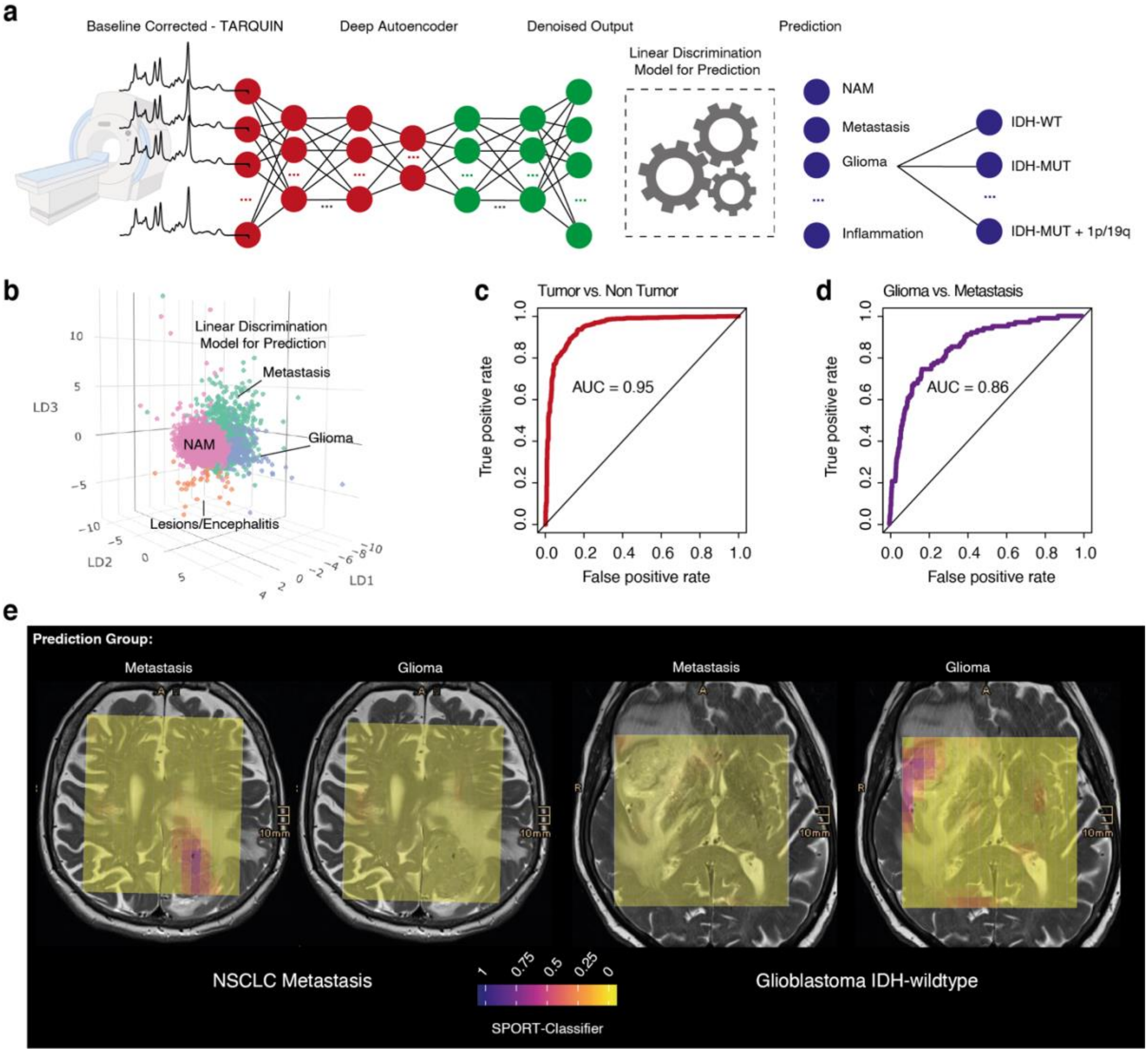

a) Workflow of our prediction model. b) 3D map of group prediction using an LDA. Colours indicate the subgroups: purple: normal-appearing matter, orange: pathological lesion (non-tumour pathology), blue: glioma and green: metastasis. c-d) Representative presentations of the AUC from our prediction model. e) Prediction maps of two patients, a metastasis (left) and an IDH-wildtype glioblastoma (right). Each voxel is coloured based on its probability to contain voxels of the predicted entity. Yellow voxels represent low prediction scores, red-purple voxels represent higher prediction scores. The colour scheme is plasma.

3.5. Exploration of metabolic diversity in pathological lesions

In order to classify the heterogeneity of pathological voxels, a subsequently isolation of the voxels that had been segmented as tumour or lesion was performed, followed by mapping of the diversity of metabolic profiles from other oncological and inflammatory brain diseases.

A frequent number of voxels could not be sharply separated between the different pathologies, except for non-Hodgkin lymphoma (NHL) and metastasis from non-small-cell lung carcinoma (NSCLC). Epidermoid tumours paired with ganglioglioma and pineal gland tumours. Voxels in the upper part of the dimensional reduction contained mostly benign lesions with highly enriched NAAG. Interestingly, a lesion histologically defined as gliosis was found to have a highly significant enrichment of aspartic acid (Asp). Molecular subgroups of glioma showed a large overlap but revealed a distinct enrichment for high-grade glioma (IDH-wildtype glioma (glioblastoma) and IDH-mutated glioma (diffuse astrocytoma WHO-Grade II and anaplastic astrocytoma WHO-Grade III)) at the bottom part of the dimensional reduction map with increased intensities for lactate (Lac), lipids and macromolecules (MM). High intensities for myoinositol (Ins) were found towards the areas assigned to NSCLC and NHL and glycerophosphocholine (GPC) significantly enriched for IDH-mutated with and without LOH (1p/19q-codeletion).

Figure 29

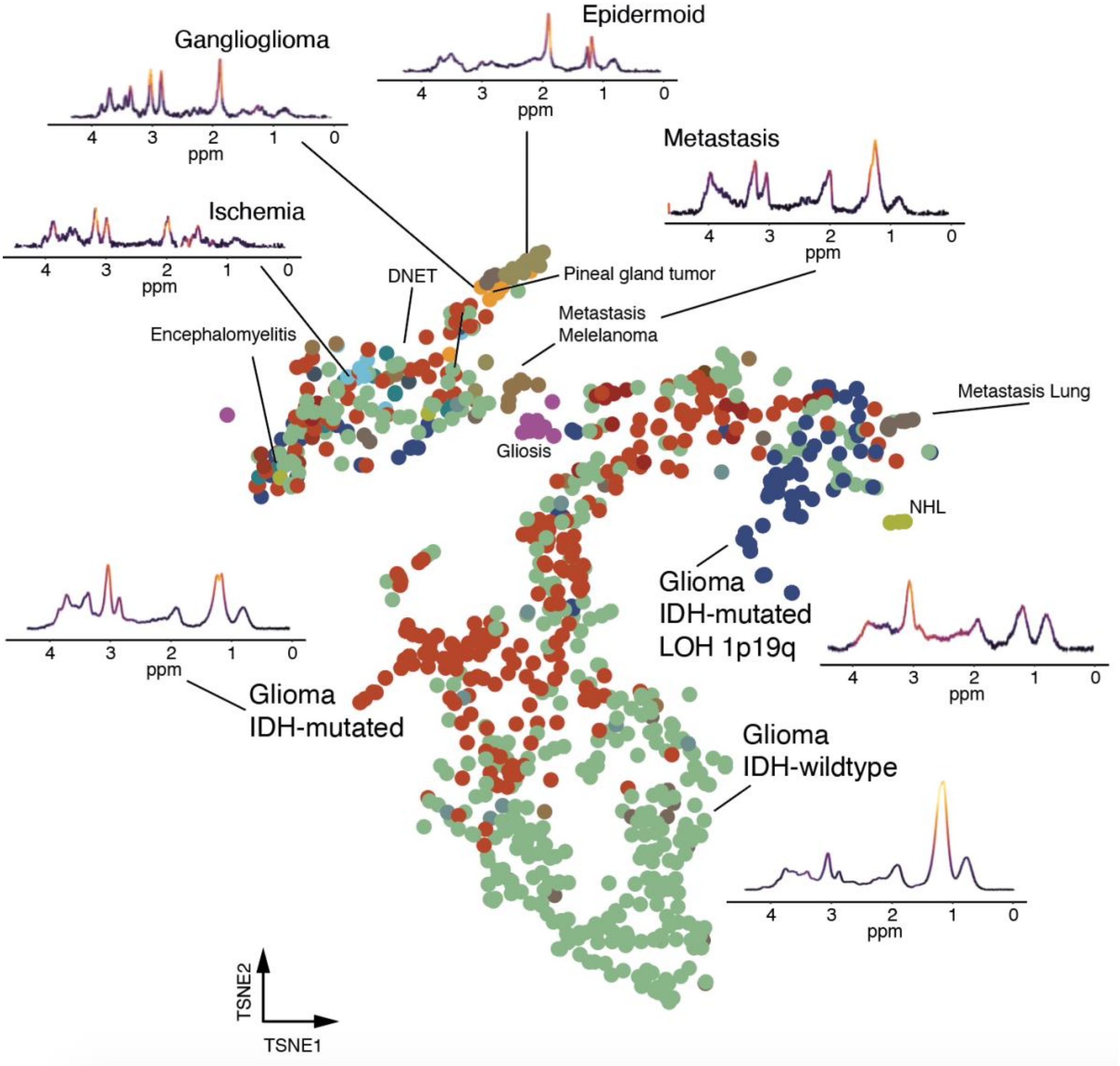

2D representation of a UMAP dimensional reduction of pathologies included in this study, representative spectra are shown.

Figure 30

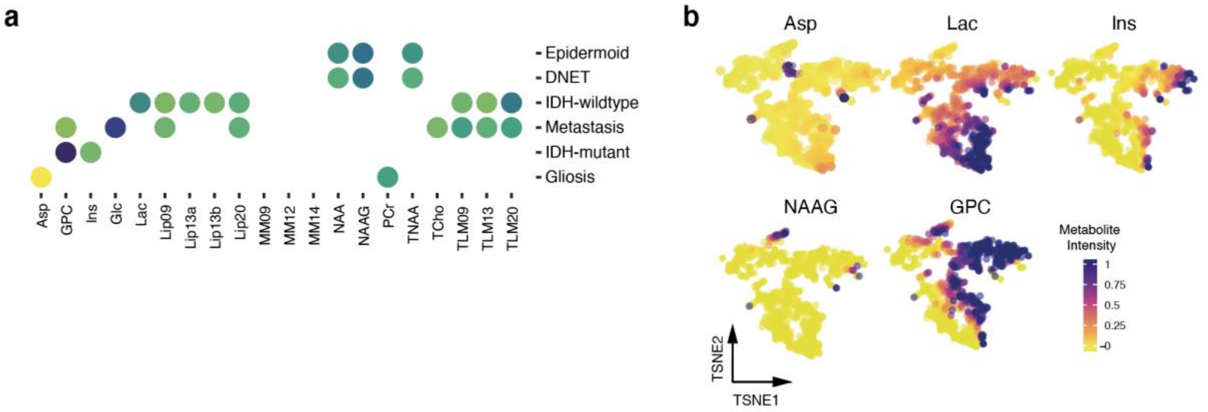

a) Dot plot of significantly enriched metabolites for each representative brain disease type. b) 2D representation of a UMAP dimensional reduction. Colours illustrate metabolite intensity.

3.6. Prediction model for molecular tumour subgroups

An LDA model was applied to train for separation between the molecular subgroups of glioma. By solely focusing on voxel from tumour regions, the model showed a high accuracy for prediction of IDH wildtype or mutated glioma, with the lowest AUC in oligodendroglioma (76.77%). It was noticeable that metabolites strongly enriched in the normal-appearing matter are considerably dominant when distinguishing between glioma subgroups, leading to an interference in the model when all voxels are considered. The prediction score (tumour subgroups) is also relatively strong in the non-tumour voxels, producing a large number of false positive predictions. To improve the overall predictive value, a two-layer model was built: layer 1 predicted a segmentation mask of those voxels with a high probability of tumour content and in layer 2 the mask was used to focus on the subtype prediction of tumour voxels exclusively.

This model enables the prediction of the molecular subgroups of patients by consideration of all pathological voxels, which resulted in a distribution of relative accuracy of all subgroups. Using this model, a 91.2% overall accuracy in predicting the molecular subtype of gliomas was achieved. Further, a spatial distribution of each score was provided, enabling the user to validate the predicted results and identify the tumour hotspot regions.

Figure 31

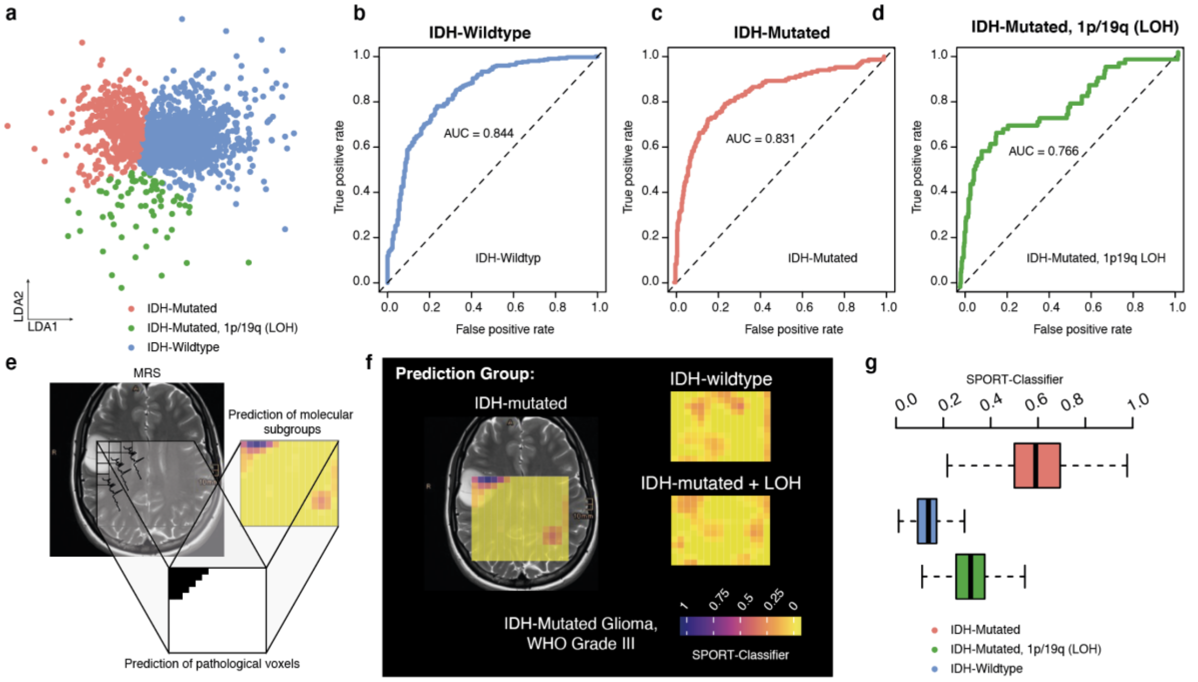

a) 2D representation of an LDA map of gliomas. b-d) AUC representations of the predictive value of each glioma subtype. e-f) Example SPORT prediction model of glioma subtypes in one patient. Each voxel is coloured based on its probability to contain voxels of the predicted entity. Yellow voxels represent low prediction scores, red-purple voxels represent higher prediction scores. The colour scheme is plasma. g) Representative SPORT classifier by summarizing all tumour voxels from level 1 prediction (layer 1) into a distribution of probabilities. The presented boxplot indicates the mean prediction score of each tumour voxel (from layer 1).

4. Discussion

The need for accurate, non-invasive diagnostic workup of brain tumours has been a crucial target in neuro-oncology over the last decades, especially since the rising importance of molecular characteristics for diagnostic and particularly for prognostic matters, with respect to expected treatment-response and survival. Many studies in neuroradiology have explored possible relations between key molecular alterations in brain tumours (such as IDH1/2-mutation, MGMT-promoter methylation on gliomas) and different features of MRI with the aid of various imaging analysis techniques and computational approaches [51–53]. Alas, most of the studies have had limited success in the accurate prediction of the molecular origin of primary brain tumours as a result of small cohorts, limited computational resources and variability in MRI data acquisition [48,54,55]. For example, Kickingereder and colleges associated radiomic features with methylation profiles and chromosomal copy number alterations but failed to prove significance for any alteration [55]. These limitations and challenges drive the motivation to find ways of improving these technologies in the future. In the last years, our group has conducted research aimed at contributing to the improvement of magnetic resonance spectroscopy, or MRS, [47,48,56–60] which allows the reconstruction of metabolic intensities in each recorded voxel. Although the technology is not novel, the possibility of expanding its use towards the prediction of molecular profiles based on metabolic diversity via unsupervised and supervised machine learning is demonstrated here.

4.1 Radiomics and Radiogenomics

The field of “omic” science [61] is based on the integrative analysis of numerous variables through dimensional reduction and machine learning algorithms. “Radiogenomics”, or “imaging genomics” describes the extraction of features, namely “radiomic features” from MRI linked to specific molecular profiles [62]. Radiomic features arise from various mathematical descriptions of pixel-wise distributions of MRI intensity within defined segments (manually or semi-manually segmented) and shape conformation measurements. The data is then fused when MR images are converted into values that can be correlated with molecular data and/or clinical parameters [63].

Various studies have shown very sharply how radiogenomics procedures based on MRI can predict defined mutational or transcriptional heterogeneity in brain tumours, but unfortunately the use of most of these approaches is in many cases limited to research purposes only due to the low reproducibility [64–66]. In general, a major limitation of radiogenomics is the variability of imaging data across scanners and MRI protocols, which highly biases the prediction models and leads to non-reproduceable results [67]. In this study, this limitation was overcome by using a standardized approach without extraction of radiomic features, as MRS inherently quantifies the metabolic diversity and predicts the intensity of up to 30 metabolites (the number of metabolites can variate according to echo times and magnetic field strength [68]). On a molecular level, our group showed a strong correlation of metabolic profiles and transcriptional heterogeneity in high-grade tumours, which suggests that MRS should be considered as the preferential imaging modality for predicting molecular alterations [56,57]. To overcome the bias of under-sampling, patients were prospectively enrolled and ~10K metabolic profiles were collected to sufficiently train the prediction models, thus overcoming the small cohort problem that can lead to insufficient training of the computational models and overfitting.

4.2 Artificial Intelligence and MRI Diagnostics

Modern technologies and artificial intelligence (AI) aid automated recognition and prediction of imaging in various medical applications [69]. Particularly in neuroradiology, many studies on predictive models based on radiomic features extracted mainly from MRI sequences have been conducted to facilitate the interpretation of diverse aspects of different brain diseases, such as brain tumours and acute stroke [54]. However, until now, the use of such techniques is not yet established [70]. In contrast to classical radiomic and radiogenomic approaches, the use of neural networks and deep learning has improved the accuracy of radiomic prediction [71]. A major challenge is the collection of sufficient training datasets, usually by manual or semi-manual segmentation of images [72]. Therefore, a web-based tool was developed to aid in the quick semi-automated segmentation of images. And for the data analysis, a deep learning autoencoder, a multi-layer neuronal network which can denoise data by reducing unnecessary information and transforming it into a normal distribution, was implemented, allowing the use of linear prediction models [49,73].

4.3 MRS in clinical use and prediction models

MRS is used in clinical setting in addition to MRI for diagnostic, prognostic and treatment response assessments, but the use of this radiological tool is not entirely widespread. Recent studies have shown the great value of the chemical and physiological information obtained from MRS in different brain pathologies and have sought to simplify its interpretation, and so MRS has gradually been incorporated in the clinical setting [48,74]. Recent studies have explored the ability of molecular subgroup prediction based on *in vivo* ^{1}HMRS in medulloblastomas [41,75] and a presurgical classification of paediatric cerebellar tumours based on metabolite ratios was successfully developed [42,76]. In adults, the same purpose has been sought. Studies have intended to establish methods based on *in-vitro* ^{1}HMRS from brain samples for classifying tumours, uncover more metabolites and thus expand the window into the biological processes behind brain tumours [77]. Nonetheless, NMR technologies and the need for specific knowledge of various analysis software for the interpretation of results can complicate the motivation for inclusion in the diagnostic process. Therefore, this study proposes a method for preoperatively characterizing and classifying brain tumours with an imaging technique that can be easily integrated in the ordinary neuroradiological routine. Based on the assumption that metabolic information is sensitive enough to detect molecular subgroups, this study aimed to use the well-known ^{1}HMR spectroscopy and modern deep-learning algorithms for characterizing of spectroscopic profiles. Following the anatomical imaging for preoperative examination of a brain lesion, patients underwent, in the same session, ^{1}HMRS imaging. Afterwards, with the aid of a custom-designed segmentation web app, the ^{1}HMRS images were semi-automatically segmented into the corresponding anatomical structures (Figure 17).

4.4 Metabolic diversity of brain tumours

Recent investigations by our group and other researchers have demonstrated the strong correlation between metabolic profiles and defined transcriptional programs in high-grade gliomas and other types of extracranial tumours [56,57,59]. In glioblastoma, tumour heterogeneity is driven by metabolic regulation of transcriptional processes and metabolic-derived selective pressure [56,57,59]. This metabolic-based information can be extrapolated non-invasively by means of MRS and translated into metabolic profiles. Hence, in this study, an unsupervised clustering of metabolic profiles was performed in order to map the landscape of metabolic diversity in malignant- and non-malignant-derived spectra. After principal component analysis, unsupervised clustering was done using the sharing nearest neighbour (SNN) algorithm which is a novel metric measure of similarity inspired by the graph-theory [78]. In the following sections, the non-malignant and malignant clusters are discussed.

4.5 Metabolic profiles of the normal appearing matter

A rather clear set of clusters marked non-malignant areas of the brain in tumour patients exhibited the highest intensities of *N*-acetyl aspartate (NAA) and creatine (Cr) (Figure 25a, c and Figure 26), which is in agreement to other findings [48,58]. As mentioned before, *N*-acetyl aspartate (NAA) is a known metabolite of neurons and has been previously described in other studies as a marker for healthy neurons [26,28,34,79]. Regarding tumour diagnostics, it has been described to have elevated levels in pilocytic astrocytoma, which can be interpreted in this case as being closer to normal brain than to malignancy [43,76]. Another metabolite which was found to be enriched in healthy brain tissue was creatine (Cr), a marker of intracellular metabolism. It has usually higher levels in grey matter. Creatine was also found to be present in the normal appearing matter-related clusters along with *N*-acetyl aspartate (NAA) (Figure 25a, c and Figure 26). Nevertheless, creatine is not a direct marker of healthy brain and usually the relevance to diagnostics of brain tumours is linked to a ratio along with choline, a more known metabolite associated with malignancy [26,31,39,76,80,81]. Recently, it was investigated that creatine directly mediates resistance against hypoxic stress in glioblastoma, which causes a transcriptional subtype switch towards proneural gene expression [56]. These findings illuminate the challenge of precisely interpreting metabolic profiles, as metabolic intensities, which are highly enriched in normal-appearing matter (NAM), may also play an important role in tumour subtype prediction. Based on this fact, a multilayer prediction model which separated NAM from any pathological profile in the first layer was established.

As previously mentioned, the prediction of NAM showed high accuracy and enabled us to analyse pathological voxels more accurately.

4.6 Metabolic profiles of brain tumours

Subsequent clustering of pathological spectra revealed clusters with high levels of choline, lactate and macromolecules (Figure 26 a), which are characteristically present in cerebral hypoxia, inflammation, cellular membrane breakdown and necrosis [26,33,76,82,83]. These clusters were the ones containing the voxels segmented to contrast-enhancement and necrotic tumour regions (Figure 25b). Typically, brain tumours exhibit a ring-shaped FLAIR hyperintensity surrounding the tumour, which in most cases is considered to be due to infiltrative tumour tissue (also seen as contrast-enhancement in the contrast-enhanced T1-weighted sequence) or oedema. Differentiating between these two provenances is rather difficult based on MRI alone. Voxels segmented as FLAIR-hyperintensity were found to be differentiated from vasogenic oedema and tumour-infiltrating regions according to their metabolic profiles (Figure 27a, b), with the first showing increased intensities of inositol, which is a metabolite known as an “osmolyte” [35], and the last showing increased intensities of malignancy-related metabolites, such as macromolecules. These results are comparable to other studies conducted for preoperatively classification of brain tumours, in paediatric and adult population [38,41–43,76,82]. These findings support that MRS is a valid tool that can discriminate between oedema regions with a suppressed intensity (ventricle-like signature) or tumour-infiltrative regions. This is of high relevance in low-grade glioma tumours where contrast-enhancement is low and a clear separation between resectable tumour and non-resectable oedematous brain tissue can be difficult based solely on MRI, which is particularly relevant from a surgical point of view. This opens a new perspective for planning of surgical procedures and may enable the surgeon to optimize the extent of resection.

4.7 Stepwise classification model for subtype prediction

As mentioned before, this study aimed to deviate from other radiomic features-based models and developed a classification algorithm combining a deep autoencoder and linear discriminant models able to predict the origin of the brain lesion (either metastatic or glial) based on metabolic profiles (Figure 28 a). As previously mentioned, the main obstacle for a well performance of metabolic classification in recent studies is the fact that metabolites are never uniquely enriched in a given subgroup. For example, in this and other studies, creatine can, on one hand, be highly enriched in normal-appearing matter, but on the other, a high intensity of creatine has also been shown to be a marker of a present IDH mutation [47,48]. To overcome this impediment, we established a multilayer model which is tailored to such limitations. This model is inspired by hierarchical denoising as used in HDBSCAN, using a layer-wise filter for spectral information which represents a hierarchical structure of classification [84]. Each layer examines the full information and is not biased by upper layers. For example, assuming that a malignant spectrum will be evaluated by our model, in the first layer the malignant nature will be predicted. The linear model in the first layer is able to detect malignant spectra with a probability of about ~98%. In the case of a positive evaluation of malignancy, the spectrum will be evaluated in the second layer in which the probability is determined whether the spectrum belongs to gliomas or another pathology. Only spectra which are predicted as gliomas will be transferred to the 3rd layer in which the molecular subgroup will be predicted.

In comparison to other published models, this approach is unique and inspired by state-of-the-art machine learning. In order to enable the use of linear models for each layer-wise prediction, a deep learning autoencoder model was chosen for transforming relatively noisy data into normal distributed data. The network architecture was then tailored with the number of bottleneck layers as well as the activation function to fully preserve the data variance represented by the eigenvector variance (Figure 18 and Figure 19). This approach was most recently established for denoising single-cell sequencing data [49].

Compared to other reported studies, the overall accuracy of this model is relatively low (~80%) due to the fact that prediction is done voxel-wise and that, in most cases, each patient has more than a single tumour voxel. The more voxel-wise predictions are performed, the higher the predictive accuracy of a patient. Here, the patient-wise prediction showed an accuracy of nearly 100%. The until-now reported prediction accuracy of this study is rather limited due to the fact that the needed validation cohort has not been enrolled yet and a 3/2 training/validation split is biased.

4.8 Outlook

This study shows that ^{1}HMRS is a non-invasive multivoxel technique that can be sufficiently applied for recording of metabolic data and is able to uncover genetic and molecular information of gliomas. By combining the metabolic and molecular traits of brain lesions, a first step towards integrating different aspects of the oncological treatment planning with the goal of improving personalized tumour treatment is described.

5. Zusammenfassung

Das hier präsentierte Projekt ermittelt die Wertigkeit metabolischer Bildgebung durch Integration artifizieller Intelligenz und maschinellem Lernen. Das Ziel ist es, die räumliche Verteilung der metabolischen Diversität im gesunden und kranken Gehirn zu kartieren und mit molekularen Eigenschaften zu korrelieren, um eine Vorhersage molekularer Tumoreigenschaften zu erlauben.

In dieser prospektiven Studie wurden zwischen 2016 und 2019 insgesamt 120 Patienten mit der räumlich-dekodierten multivoxel Protonenspektroskopie (^{1}HMRS) eingeschlossen. Innerhalb einer explorativen Analyse konnten wir mit Hilfe nicht supervisiertem Lernen die metabolische Diversität aufzeigen. Hierbei identifizierten wir Metaboliten wie N-Acetyl-Aspartat und Kreatin, die eindeutigen Prädiktoren gesunder Hirnteile darstellten. Wir identifizierten metabolische Signaturen, die einzigartig für verschiedene molekulare Subtypen sind. Diese Ergebnisse nutzten wir zur Entwicklung eines Vorhersagemodels, das anhand der aufgenommenen Spektren die Wahrscheinlichkeit einzelner molekularen Subgruppen bestimmen kann. Mithilfe unserer gewonnenen Erkenntnisse sind wir in Zukunft in der Lage, eine robuste Vorhersage molekularer Subgruppen bei Gliomen bereits präoperativ vornehmen zu können.

Summary

In this project, the significance of metabolic imaging by integrating artificial intelligence and machine learning was investigated. The goal is to map the spatial distribution of the metabolic diversity of the brain in health and disease and correlate these findings with molecular profiles, allowing the non-invasively prediction of molecular tumour characteristics.

In this prospective study, a total of 120 patients were enrolled between 2016 and 2019 who received spatial decoded multivoxel proton spectroscopy (*in-vivo* ^{1}HMRS). The exploratory analysis revealed the metabolic diversity of the healthy and diseased brain using non-supervised learning. Metabolites such as N-acetyl-aspartate and creatine were identified, which were clear predictors of healthy brain parts. Metabolic signatures unique to different molecular subtypes were described. These results were used to develop a predictive model that can determine the likelihood of individual molecular subgroups based on the recorded spectra. With the help of these findings, a robust prediction of molecular subgroups in gliomas already preoperatively will be refined.

6. References

1. Bell, J. S.; Koffie, R. M.; Rattani, A.; Dewan, M. C.; Baticulon, R. E.; Qureshi, M. M.; Wahjoepramono, E. J.; Rosseau, G.; Park, K.; Nahed, B. V. Global incidence of brain and spinal tumors by geographic region and income level based on cancer registry data. *J. Clin. Neurosci.* **2019**, *66*, 121–127.

2. Miranda-Filho, A.; Piñeros, M.; Soerjomataram, I.; Deltour, I.; Bray, F. Cancers of the brain and CNS: global patterns and trends in incidence. *Neuro. Oncol.* **2017**, *19*, 270–280.

3. GBD 2016 Brain and Other CNS Cancer Collaborators Global, regional, and national burden of brain and other CNS cancer, 1990-2016: a systematic analysis for the Global Burden of Disease Study 2016. *Lancet Neurol.* **2019**, *18*, 376–393.

4. Ostrom, Q. T.; Cioffi, G.; Gittleman, H.; Patil, N.; Waite, K.; Kruchko, C.; Barnholtz-Sloan, J. S. CBTRUS Statistical Report: Primary Brain and Other Central Nervous System Tumors Diagnosed in the United States in 2012-2016. *Neuro. Oncol.* **2019**, *21*, v1–v100.

5. Barnholtz-Sloan, J. S.; Ostrom, Q. T.; Cote, D. Epidemiology of brain tumors. *Neurol. Clin.* **2018**, *36*, 395–419.

6. Rosati, A.; Tomassini, A.; Pollo, B.; Ambrosi, C.; Schwarz, A.; Padovani, A.; Bonetti, B. Epilepsy in cerebral glioma: timing of appearance and histological correlations. *J. Neurooncol.* **2009**, *93*, 395–400.

7. Greenberg, M. S.; Abel, N.; Agazzi, S. *Handbook of Neurosurgery*; Georg Thieme Verlag, 2020.

8. Stupp, R.; Mason, W. P.; van den Bent, M. J.; Weller, M.; Fisher, B.; Taphoorn, M. J. B.; Belanger, K.; Brandes, A. A.; Marosi, C.; Bogdahn, U.; Curschmann, J.; Janzer, R. C.; Ludwin, S. K.; Gorlia, T.; Allgeier, A.; Lacombe, D.; Cairncross, J. G.; Eisenhauer, E.; Mirimanoff, R. O.; European Organisation for Research and Treatment of Cancer Brain Tumor and Radiotherapy Groups; National Cancer Institute of Canada Clinical Trials Group Radiotherapy plus concomitant and adjuvant temozolomide for glioblastoma. *N. Engl. J. Med.* **2005**, *352*, 987–996.

9. Weller, M.; Wick, W.; Aldape, K.; Brada, M.; Berger, M.; Pfister, S. M.; Nishikawa, R.; Rosenthal, M.; Wen, P. Y.; Stupp, R.; Reifenberger, G. Glioma. *Nat. Rev. Dis. Primers* **2015**, *1*, 15017.

10. Schalper, K. A.; Rodriguez-Ruiz, M. E.; Diez-Valle, R.; López-Janeiro, A.; Porciuncula, A.; Idoate, M. A.; Inogés, S.; de Andrea, C.; López-Diaz de Cerio, A.; Tejada, S.; Berraondo, P.; Villarroel-Espindola, F.; Choi, J.; Gúrpide, A.; Giraldez, M.; Goicoechea, I.; Gallego

Perez-Larraya, J.; Sanmamed, M. F.; Perez-Gracia, J. L.; Melero, I. Neoadjuvant nivolumab modifies the tumor immune microenvironment in resectable glioblastoma. *Nat. Med.* **2019**, *25*, 470–476.

11. Cloughesy, T. F.; Mochizuki, A. Y.; Orpilla, J. R.; Hugo, W.; Lee, A. H.; Davidson, T. B.; Wang, A. C.; Ellingson, B. M.; Rytlewski, J. A.; Sanders, C. M.; Kawaguchi, E. S.; Du, L.; Li, G.; Yong, W. H.; Gaffey, S. C.; Cohen, A. L.; Mellinghoff, I. K.; Lee, E. Q.; Reardon, D. A.; O'Brien, B. J.; Butowski, N. A.; Nghiemphu, P. L.; Clarke, J. L.; Arrillaga-Romany, I. C.; Colman, H.; Kaley, T. J.; de Groot, J. F.; Liau, L. M.; Wen, P. Y.; Prins, R. M. Neoadjuvant anti-PD-1 immunotherapy promotes a survival benefit with intratumoral and systemic immune responses in recurrent glioblastoma. *Nat. Med.* **2019**, *25*, 477–486.

12. Ho, V. K. Y.; Reijneveld, J. C.; Enting, R. H.; Bienfait, H. P.; Robe, P.; Baumert, B. G.; Visser, O.; Dutch Society for Neuro-Oncology (LWNO) Changing incidence and improved survival of gliomas. *Eur. J. Cancer* **2014**, *50*, 2309–2318.

13. Roelz, R.; Strohmaier, D.; Jabbarli, R.; Kraeutle, R.; Egger, K.; Coenen, V. A.; Weyerbrock, A.; Reinacher, P. C. Residual Tumor Volume as Best Outcome Predictor in Low Grade Glioma - A Nine-Years Near-Randomized Survey of Surgery vs. Biopsy. *Sci. Rep.* **2016**, *6*, 32286.

14. Buckner, J. C.; Shaw, E. G.; Pugh, S. L.; Chakravarti, A.; Gilbert, M. R.; Barger, G. R.; Coons, S.; Ricci, P.; Bullard, D.; Brown, P. D.; Stelzer, K.; Brachman, D.; Suh, J. H.; Schultz, C. J.; Bahary, J.-P.; Fisher, B. J.; Kim, H.; Murtha, A. D.; Bell, E. H.; Won, M.; Mehta, M. P.; Curran, W. J. Radiation plus Procarbazine, CCNU, and Vincristine in Low-Grade Glioma. *N. Engl. J. Med.* **2016**, *374*, 1344–1355.

15. Sanai, N.; Berger, M. S. Surgical oncology for gliomas: the state of the art. *Nat. Rev. Clin. Oncol.* **2018**, *15*, 112–125.

16. Louis, D. N.; Perry, A.; Reifenberger, G.; von Deimling, A.; Figarella-Branger, D.; Cavenee, W. K.; Ohgaki, H.; Wiestler, O. D.; Kleihues, P.; Ellison, D. W. The 2016 World Health Organization Classification of Tumors of the Central Nervous System: a summary. *Acta Neuropathol.* **2016**, *131*, 803–820.

17. Molinaro, A. M.; Taylor, J. W.; Wiencke, J. K.; Wrensch, M. R. Genetic and molecular epidemiology of adult diffuse glioma. *Nat. Rev. Neurol.* **2019**, *15*, 405–417.

18. Yan, H.; Parsons, D. W.; Jin, G.; McLendon, R.; Rasheed, B. A.; Yuan, W.; Kos, I.; Batinic-Haberle, I.; Jones, S.; Riggins, G. J.; Friedman, H.; Friedman, A.; Reardon, D.; Herndon, J.; Kinzler, K. W.; Velculescu, V. E.; Vogelstein, B.; Bigner, D. D. IDH1 and IDH2 mutations in gliomas. *N. Engl. J. Med.* **2009**, *360*, 765–773.

19. Yang, H.; Ye, D.; Guan, K.-L.; Xiong, Y. IDH1 and IDH2 mutations in tumorigenesis: mechanistic insights and clinical perspectives. *Clin. Cancer Res.* **2012**, *18*, 5562–5571.

20. Ostrom, Q. T.; Gittleman, H.; Liao, P.; Vecchione-Koval, T.; Wolinsky, Y.; Kruchko, C.; Barnholtz-Sloan, J. S. CBTRUS Statistical Report: Primary brain and other central nervous system tumors diagnosed in the United States in 2010-2014. *Neuro. Oncol.* **2017**, *19*, v1–v88.

21. Crespo, I.; Vital, A. L.; Nieto, A. B.; Rebelo, O.; Tão, H.; Lopes, M. C.; Oliveira, C. R.; French, P. J.; Orfao, A.; Tabernero, M. D. Detailed characterization of alterations of chromosomes 7, 9, and 10 in glioblastomas as assessed by single-nucleotide polymorphism arrays. *J Mol Diagn* **2011**, *13*, 634–647.

22. Hegi, M. E.; Diserens, A.-C.; Gorlia, T.; Hamou, M.-F.; de Tribolet, N.; Weller, M.; Kros, J. M.; Hainfellner, J. A.; Mason, W.; Mariani, L.; Bromberg, J. E. C.; Hau, P.; Mirimanoff, R. O.; Cairncross, J. G.; Janzer, R. C.; Stupp, R. MGMT gene silencing and benefit from temozolomide in glioblastoma. *N. Engl. J. Med.* **2005**, *352*, 997–1003.

23. Schreck, K. C.; Grossman, S. A.; Pratilas, C. A. BRAF mutations and the utility of RAF and MEK inhibitors in primary brain tumors. *Cancers (Basel)* **2019**, *11*.

24. Karsy, M.; Guan, J.; Cohen, A. L.; Jensen, R. L.; Colman, H. New molecular considerations for glioma: IDH, ATRX, BRAF, TERT, H3 K27M. *Curr Neurol Neurosci Rep* **2017**, *17*, 19.

25. Mader, I.; Roser, W.; Hagberg, G.; Schneider, M.; Sauter, R.; Seelig, J.; Radue, E. W.; Steinbrich, W. Proton chemical shift imaging, metabolic maps, and single voxel spectroscopy of glial brain tumors. *MAGMA* **1996**, *4*, 139–150.

26. Bertholdo, D.; Watcharakorn, A.; Castillo, M. Brain proton magnetic resonance spectroscopy: introduction and overview. *Neuroimaging Clin. N. Am.* **2013**, *23*, 359–380.

27. van der Graaf, M. In vivo magnetic resonance spectroscopy: basic methodology and clinical applications. *Eur Biophys J* **2010**, *39*, 527–540.

28. Hajek, M.; Dezortova, M. Introduction to clinical in vivo MR spectroscopy. *Eur. J. Radiol.* **2008**, *67*, 185–193.

29. Hellström, J.; Romanos Zapata, R.; Libard, S.; Wikström, J.; Ortiz-Nieto, F.; Alafuzoff, I.; Raininko, R. The value of magnetic resonance spectroscopy as a supplement to MRI of the brain in a clinical setting. *PLoS One* **2018**, *13*, e0207336.

30. Kwock, L.; Smith, J. K.; Castillo, M.; Ewend, M. G.; Cush, S.; Hensing, T.; Varia, M.; Morris, D.; Bouldin, T. W. Clinical applications of proton MR spectroscopy in oncology. *Technol Cancer Res Treat* **2002**, *1*, 17–28.

31. Dowling, C.; Bollen, A. W.; Noworolski, S. M.; McDermott, M. W.; Barbaro, N. M.;

Day, M. R.; Henry, R. G.; Chang, S. M.; Dillon, W. P.; Nelson, S. J.; Vigneron, D. B. Preoperative proton MR spectroscopic imaging of brain tumors: correlation with histopathologic analysis of resection specimens. *AJNR Am. J. Neuroradiol.* **2001**, *22*, 604–612.

32. Oz, G.; Alger, J. R.; Barker, P. B.; Bartha, R.; Bizzi, A.; Boesch, C.; Bolan, P. J.; Brindle, K. M.; Cudalbu, C.; Dinçer, A.; Dydak, U.; Emir, U. E.; Frahm, J.; González, R. G.; Gruber, S.; Gruetter, R.; Gupta, R. K.; Heerschap, A.; Henning, A.; Hetherington, H. P.; Howe, F. A.; Hüppi, P. S.; Hurd, R. E.; Kantarci, K.; Klomp, D. W. J.; Kreis, R.; Kruiskamp, M. J.; Leach, M. O.; Lin, A. P.; Luijten, P. R.; Marjańska, M.; Maudsley, A. A.; Meyerhoff, D. J.; Mountford, C. E.; Nelson, S. J.; Pamir, M. N.; Pan, J. W.; Peet, A. C.; Poptani, H.; Posse, S.; Pouwels, P. J. W.; Ratai, E.-M.; Ross, B. D.; Scheenen, T. W.; Schuster, C.; Smith, I. C. P.; Soher, B. J.; Tkáč, I.; Vigneron, D. B.; Kauppinen, R. A.; MRS Consensus Group Clinical proton MR spectroscopy in central nervous system disorders. *Radiology* **2014**, *270*, 658–679.

33. Mader, I.; Rauer, S.; Gall, P.; Klose, U. (1)H MR spectroscopy of inflammation, infection and ischemia of the brain. *Eur. J. Radiol.* **2008**, *67*, 250–257.

34. Lin, A.; Ross, B. D.; Harris, K.; Wong, W. Efficacy of proton magnetic resonance spectroscopy in neurological diagnosis and neurotherapeutic decision making. *NeuroRx* **2005**, *2*, 197–214.

35. Haris, M.; Cai, K.; Singh, A.; Hariharan, H.; Reddy, R. In vivo mapping of brain myo-inositol. *Neuroimage* **2011**, *54*, 2079–2085.

36. Castillo, M.; Smith, J. K.; Kwock, L. Correlation of myo-inositol levels and grading of cerebral astrocytomas. *AJNR Am. J. Neuroradiol.* **2000**, *21*, 1645–1649.

37. Mader, I.; Roser, W.; Hagberg, G.; Schneider, M.; Sauter, R.; Seelig, J.; Radue, E. W.; Steinbrich, W. Proton chemical shift imaging, metabolic maps, and single voxel spectroscopy of glial brain tumors. *MAGMA* **1996**, *4*, 139–150.

38. Manias, K.; Gill, S. K.; Zarinabad, N.; Davies, P.; English, M.; Ford, D.; MacPherson, L.; Nicklaus-Wollenteit, I.; Oates, A.; Solanki, G.; Adamski, J.; Wilson, M.; Peet, A. C. Evaluation of the added value of 1H-magnetic resonance spectroscopy for the diagnosis of pediatric brain lesions in clinical practice. *Neurooncol Pract* **2018**, *5*, 18–27.

39. Bulik, M.; Jancalek, R.; Vanicek, J.; Skoch, A.; Mechl, M. Potential of MR spectroscopy for assessment of glioma grading. *Clin. Neurol. Neurosurg.* **2013**, *115*, 146–153.

40. Horská, A.; Barker, P. B. Imaging of brain tumors: MR spectroscopy and metabolic imaging. *Neuroimaging Clin. N. Am.* **2010**, *20*, 293–310.

41. Blüml, S.; Margol, A. S.; Sposto, R.; Kennedy, R. J.; Robison, N. J.; Vali, M.; Hung, L.

T.; Muthugounder, S.; Finlay, J. L.; Erdreich-Epstein, A.; Gilles, F. H.; Judkins, A. R.; Krieger, M. D.; Dhall, G.; Nelson, M. D.; Asgharzadeh, S. Molecular subgroups of medulloblastoma identification using noninvasive magnetic resonance spectroscopy. *Neuro. Oncol.* **2016**, *18*, 126–131.

42. Manias, K. A.; Harris, L. M.; Davies, N. P.; Natarajan, K.; MacPherson, L.; Foster, K.; Brundler, M.-A.; Hargrave, D. R.; Payne, G. S.; Leach, M. O.; Morgan, P. S.; Auer, D.; Jaspan, T.; Arvanitis, T. N.; Grundy, R. G.; Peet, A. C. Prospective multicentre evaluation and refinement of an analysis tool for magnetic resonance spectroscopy of childhood cerebellar tumours. *Pediatr Radiol* **2018**, *48*, 1630–1641.

43. Zarinabad, N.; Abernethy, L. J.; Avula, S.; Davies, N. P.; Rodriguez Gutierrez, D.; Jaspan, T.; MacPherson, L.; Mitra, D.; Rose, H. E. L.; Wilson, M.; Morgan, P. S.; Bailey, S.; Pizer, B.; Arvanitis, T. N.; Grundy, R. G.; Auer, D. P.; Peet, A. Application of pattern recognition techniques for classification of pediatric brain tumors by in vivo 3T 1 H-MR spectroscopy-A multi-center study. *Magn. Reson. Med.* **2018**, *79*, 2359–2366.

44. Wilson, M.; Cummins, C. L.; Macpherson, L.; Sun, Y.; Natarajan, K.; Grundy, R. G.; Arvanitis, T. N.; Kauppinen, R. A.; Peet, A. C. Magnetic resonance spectroscopy metabolite profiles predict survival in paediatric brain tumours. *Eur. J. Cancer* **2013**, *49*, 457–464.

45. Choi, C.; Ganji, S. K.; DeBerardinis, R. J.; Hatanpaa, K. J.; Rakheja, D.; Kovacs, Z.; Yang, X.-L.; Mashimo, T.; Raisanen, J. M.; Marin-Valencia, I.; Pascual, J. M.; Madden, C. J.; Mickey, B. E.; Malloy, C. R.; Bachoo, R. M.; Maher, E. A. 2-hydroxyglutarate detection by magnetic resonance spectroscopy in IDH-mutated patients with gliomas. *Nat. Med.* **2012**, *18*, 624–629.

46. Laino, M. E.; Young, R.; Beal, K.; Haque, S.; Mazaheri, Y.; Corrias, G.; Bitencourt, A. G.; Karimi, S.; Thakur, S. B. Magnetic resonance spectroscopic imaging in gliomas: clinical diagnosis and radiotherapy planning. *BJR Open* **2020**, *2*, 20190026.

47. Heiland, D. H.; Mader, I.; Schlosser, P.; Pfeifer, D.; Carro, M. S.; Lange, T.; Schwarzwald, R.; Vasilikos, I.; Urbach, H.; Weyerbrock, A. Integrative Network-based Analysis of Magnetic Resonance Spectroscopy and Genome Wide Expression in Glioblastoma multiforme. *Sci. Rep.* **2016**, *6*, 29052.

48. Diamandis, E.; Gabriel, C. P. S.; Würtemberger, U.; Guggenberger, K.; Urbach, H.; Staszewski, O.; Lassmann, S.; Schnell, O.; Grauvogel, J.; Mader, I.; Heiland, D. H. MR-spectroscopic imaging of glial tumors in the spotlight of the 2016 WHO classification. *J. Neurooncol.* **2018**, *139*, 431–440.

49. Eraslan, G.; Simon, L. M.; Mircea, M.; Mueller, N. S.; Theis, F. J. Single-cell RNA-seq

denoising using a deep count autoencoder. *Nat. Commun.* **2019**, *10*, 390.

50. Kueckelhaus, J.; Ehr, J. von; Ravi, V. M.; Will, P.; Joseph, K. M.; Beck, J.; Hofmann, U. G.; Delev, D.; Schnell, O.; Heiland, H. D. Inferring spatially transient gene expression pattern from spatial transcriptomic studies. *BioRxiv* **2020**.

51. Tejada Neyra, M. A.; Neuberger, U.; Reinhardt, A.; Brugnara, G.; Bonekamp, D.; Sill, M.; Wick, A.; Jones, D. T. W.; Radbruch, A.; Unterberg, A.; Debus, J.; Heiland, S.; Schlemmer, H.-P.; Herold-Mende, C.; Pfister, S.; von Deimling, A.; Wick, W.; Capper, D.; Bendszus, M.; Kickingereder, P. Voxel-wise radiogenomic mapping of tumor location with key molecular alterations in patients with glioma. *Neuro. Oncol.* **2018**, *20*, 1517–1524.

52. Wiestler, B.; Capper, D.; Hovestadt, V.; Sill, M.; Jones, D. T. W.; Hartmann, C.; Felsberg, J.; Platten, M.; Feiden, W.; Keyvani, K.; Pfister, S. M.; Wiestler, O. D.; Meyermann, R.; Reifenberger, G.; Pietsch, T.; von Deimling, A.; Weller, M.; Wick, W. Assessing CpG island methylator phenotype, 1p/19q codeletion, and MGMT promoter methylation from epigenome-wide data in the biomarker cohort of the NOA-04 trial. *Neuro. Oncol.* **2014**, *16*, 1630–1638.

53. Kickingereder, P.; Sahm, F.; Radbruch, A.; Wick, W.; Heiland, S.; Deimling, A. von; Bendszus, M.; Wiestler, B. IDH mutation status is associated with a distinct hypoxia/angiogenesis transcriptome signature which is non-invasively predictable with rCBV imaging in human glioma. *Sci. Rep.* **2015**, *5*, 16238.

54. Kickingereder, P.; Neuberger, U.; Bonekamp, D.; Piechotta, P. L.; Götz, M.; Wick, A.; Sill, M.; Kratz, A.; Shinohara, R. T.; Jones, D. T. W.; Radbruch, A.; Muschelli, J.; Unterberg, A.; Debus, J.; Schlemmer, H.-P.; Herold-Mende, C.; Pfister, S.; von Deimling, A.; Wick, W.; Capper, D.; Maier-Hein, K. H.; Bendszus, M. Radiomic subtyping improves disease stratification beyond key molecular, clinical, and standard imaging characteristics in patients with glioblastoma. *Neuro. Oncol.* **2018**, *20*, 848–857.

55. Kickingereder, P.; Bonekamp, D.; Nowosielski, M.; Kratz, A.; Sill, M.; Burth, S.; Wick, A.; Eidel, O.; Schlemmer, H.-P.; Radbruch, A.; Debus, J.; Herold-Mende, C.; Unterberg, A.; Jones, D.; Pfister, S.; Wick, W.; von Deimling, A.; Bendszus, M.; Capper, D. Radiogenomics of Glioblastoma: Machine Learning-based Classification of Molecular Characteristics by Using Multiparametric and Multiregional MR Imaging Features. *Radiology* **2016**, *281*, 907–918.

56. Heiland, D. H.; Gaebelein, A.; Börries, M.; Wörner, J.; Pompe, N.; Franco, P.; Heynckes, S.; Bartholomae, M.; hAilín, D. Ó.; Carro, M. S.; Prinz, M.; Weber, S.; Mader, I.; Delev, D.; Schnell, O. Microenvironment-Derived Regulation of HIF Signaling Drives Transcriptional

Heterogeneity in Glioblastoma Multiforme. *Mol. Cancer Res.* **2018**, *16*, 655–668.

57. Heiland, D. H.; Wörner, J.; Haaker, J. G.; Delev, D.; Pompe, N.; Mercas, B.; Franco, P.; Gäbelein, A.; Pfeifer, D.; Weber, S.; Mader, I.; Schnell, O. The integrative metabolomic-transcriptomic glioblastome multiforme landscape of. *Oncotarget* **2017**.

58. Demerath, T.; Simon-Gabriel, C. P.; Kellner, E.; Schwarzwald, R.; Lange, T.; Heiland, D. H.; Reinacher, P.; Staszewski, O.; Mast, H.; Kiselev, V. G.; Egger, K.; Urbach, H.; Weyerbrock, A.; Mader, I. Mesoscopic imaging of glioblastomas: Are diffusion, perfusion and spectroscopic measures influenced by the radiogenetic phenotype? *Neuroradiol. J.* **2017**, *30*, 36–47.

59. Heiland, D. H.; Wörner, J.; Gerrit Haaker, J.; Delev, D.; Pompe, N.; Mercas, B.; Franco, P.; Gäbelein, A.; Heynckes, S.; Pfeifer, D.; Weber, S.; Mader, I.; Schnell, O. The integrative metabolomic-transcriptomic landscape of glioblastome multiforme. *Oncotarget* **2017**, *8*, 49178–49190.

60. Heiland, D. H.; Ferrarese, R.; Claus, R.; Dai, F.; Masilamani, A. P.; Kling, E.; Weyerbrock, A.; Kling, T.; Nelander, S.; Carro, M. S. c-Jun-N-terminal phosphorylation regulates DNMT1 expression and genome wide methylation in gliomas. *Oncotarget* **2017**, *8*, 6940–6954.

61. Quackenbush, J. Data standards for “omic” science. *Nat. Biotechnol.* **2004**, *22*, 613–614.

62. Traverso, A.; Wee, L.; Dekker, A.; Gillies, R. Repeatability and reproducibility of radiomic features: A systematic review. *Int. J. Radiat. Oncol. Biol. Phys.* **2018**, *102*, 1143–1158.

63. Shen, L.; Thompson, P. M. Brain imaging genomics: integrated analysis and machine learning. *Proc IEEE Inst Electr Electron Eng* **2020**, *108*, 125–162.

64. Kickingereder, P.; Isensee, F.; Tursunova, I.; Petersen, J.; Neuberger, U.; Bonekamp, D.; Brugnara, G.; Schell, M.; Kessler, T.; Foltyn, M.; Harting, I.; Sahm, F.; Prager, M.; Nowosielski, M.; Wick, A.; Nolden, M.; Radbruch, A.; Debus, J.; Schlemmer, H.-P.; Heiland, S.; Platten, M.; von Deimling, A.; van den Bent, M. J.; Gorlia, T.; Wick, W.; Bendszus, M.; Maier-Hein, K. H. Automated quantitative tumour response assessment of MRI in neuro-oncology with artificial neural networks: a multicentre, retrospective study. *Lancet Oncol.* **2019**, *20*, 728–740.

65. Park, C. J.; Han, K.; Kim, H.; Ahn, S. S.; Choi, D.; Park, Y. W.; Chang, J. H.; Kim, S. H.; Cha, S.; Lee, S. K. MRI Features May Predict Molecular Features of Glioblastoma in Isocitrate Dehydrogenase Wild-Type Lower-Grade Gliomas. *AJNR Am. J. Neuroradiol.* **2021**.

66. Binder, Z. A.; Thorne, A. H.; Bakas, S.; Wileyto, E. P.; Bilello, M.; Akbari, H.; Rathore, S.; Ha, S. M.; Zhang, L.; Ferguson, C. J.; Dahiya, S.; Bi, W. L.; Reardon, D. A.; Idbaih, A.; Felsberg, J.; Hentschel, B.; Weller, M.; Bagley, S. J.; Morrissette, J. J. D.; Nasrallah, M. P.; Ma, J.; Zanca, C.; Scott, A. M.; Orellana, L.; Davatzikos, C.; Furnari, F. B.; O'Rourke, D. M. Epidermal growth factor receptor extracellular domain mutations in glioblastoma present opportunities for clinical imaging and therapeutic development. *Cancer Cell* **2018**, *34*, 163–177.e7.

67. Zhovannik, I.; Bussink, J.; Traverso, A.; Shi, Z.; Kalendralis, P.; Wee, L.; Dekker, A.; Fijten, R.; Monshouwer, R. Learning from scanners: Bias reduction and feature correction in radiomics. *Clinical and Translational Radiation Oncology* **2019**, *19*, 33–38.

68. Mekle, R.; Mlynárik, V.; Gambarota, G.; Hergt, M.; Krueger, G.; Gruetter, R. MR spectroscopy of the human brain with enhanced signal intensity at ultrashort echo times on a clinical platform at 3T and 7T. *Magn. Reson. Med.* **2009**, *61*, 1279–1285.

69. Wang, F.; Casalino, L. P.; Khullar, D. Deep Learning in Medicine-Promise, Progress, and Challenges. *JAMA Intern. Med.* **2019**, *179*, 293–294.

70. Peet, A. C.; Arvanitis, T. N.; Leach, M. O.; Waldman, A. D. Functional imaging in adult and paediatric brain tumours. *Nat. Rev. Clin. Oncol.* **2012**, *9*, 700–711.

71. Afshar, P.; Mohammadi, A.; Plataniotis, K. N.; Oikonomou, A.; Benali, H. From Handcrafted to Deep-Learning-Based Cancer Radiomics: Challenges and opportunities. *IEEE Signal Process. Mag.* **2019**, *36*, 132–160.

72. Ibrahim, A.; Primakov, S.; Beuque, M.; Woodruff, H. C.; Halilaj, I.; Wu, G.; Refaee, T.; Granzier, R.; Widaatalla, Y.; Hustinx, R.; Mottaghy, F. M.; Lambin, P. Radiomics for precision medicine: Current challenges, future prospects, and the proposal of a new framework. *Methods* **2020**.

73. Gondara, L. Medical image denoising using convolutional denoising autoencoders. *2016 IEEE 16th International Conference on Data* **2016**.

74. Dikaios, N. Deep learning magnetic resonance spectroscopy fingerprints of brain tumours using quantum mechanically synthesised data. *NMR Biomed.* **2021**, e4479.

75. Perreault, S.; Ramaswamy, V.; Achrol, A. S.; Chao, K.; Liu, T. T.; Shih, D.; Remke, M.; Schubert, S.; Bouffet, E.; Fisher, P. G.; Partap, S.; Vogel, H.; Taylor, M. D.; Cho, Y. J.; Yeom, K. W. MRI surrogates for molecular subgroups of medulloblastoma. *AJNR Am. J. Neuroradiol.* **2014**, *35*, 1263–1269.

76. Harris, L. M.; Davies, N.; Macpherson, L.; Foster, K.; Lateef, S.; Natarajan, K.; Sgouros, S.; Brundler, M.-A.; Arvanitis, T. N.; Grundy, R. G.; Peet, A. C. The use of short-echo-time

1H MRS for childhood cerebellar tumours prior to histopathological diagnosis. *Pediatr Radiol* **2007**, *37*, 1101–1109.

77. Andronesi, O. C.; Blekas, K. D.; Mintzopoulos, D.; Astrakas, L.; Black, P. M.; Tzika, A. A. Molecular classification of brain tumor biopsies using solid-state magic angle spinning proton magnetic resonance spectroscopy and robust classifiers. *Int. J. Oncol.* **2008**, *33*, 1017–1025.

78. Jarvis, R. A.; Patrick, E. A. Clustering Using a Similarity Measure Based on Shared Near Neighbors. *IEEE Trans. Comput.* **1973**, *C-22*, 1025–1034.

79. Chaumeil, M. M.; Lupo, J. M.; Ronen, S. M. Magnetic resonance (MR) metabolic imaging in glioma. *Brain Pathol.* **2015**, *25*, 769–780.

80. Kickingereder, P.; Götz, M.; Muschelli, J.; Wick, A.; Neuberger, U.; Shinohara, R. T.; Sill, M.; Nowosielski, M.; Schlemmer, H.-P.; Radbruch, A.; Wick, W.; Bendszus, M.; Maier-Hein, K. H.; Bonekamp, D. Large-scale Radiomic Profiling of Recurrent Glioblastoma Identifies an Imaging Predictor for Stratifying Anti-Angiogenic Treatment Response. *Clin. Cancer Res.* **2016**, *22*, 5765–5771.

81. Shimizu, H.; Kumabe, T.; Shirane, R.; Yoshimoto, T. Correlation between choline level measured by proton MR spectroscopy and Ki-67 labeling index in gliomas. *AJNR Am. J. Neuroradiol.* **2000**, *21*, 659–665.

82. Durmo, F.; Rydelius, A.; Cuellar Baena, S.; Askaner, K.; Lätt, J.; Bengzon, J.; Englund, E.; Chenevert, T. L.; Björkman-Burtscher, I. M.; Sundgren, P. C. Multivoxel 1H-MR Spectroscopy Biometrics for Preoprerative Differentiation Between Brain Tumors. *Tomography* **2018**, *4*, 172–181.

83. Majós, C.; Aguilera, C.; Alonso, J.; Julià-Sapé, M.; Castañer, S.; Sánchez, J. J.; Samitier, A.; León, A.; Rovira, A.; Arús, C. Proton MR spectroscopy improves discrimination between tumor and pseudotumoral lesion in solid brain masses. *AJNR Am. J. Neuroradiol.* **2009**, *30*, 544–551.

84. McInnes, L.; Healy, J.; Astels, S. hdbscan: Hierarchical density based clustering. *JOSS* **2017**, *2*, 205.

Curriculum vitae

This page contains personal data. It is therefore not part of the online publication.

Diese Seite enthält persönliche Daten. Sie ist deshalb nicht Bestandteil der Online-Veröffentlichung.

Publications

Franco P., Huebschle, I., Simon-Gabriel, C.P., Dacca, K., Schnell, O., Beck, J., Mast, H., Urbach, H., Wuerttemberger, U., Prinz, M., Hosp, J.A., Delev, D., Mader, I., Heiland, D.H. Mapping of Metabolic Heterogeneity of Glioma using MR-Spectroscopy. Cancers (Basel). 2021 May 17;13(10):2417. doi: 10.3390/cancers13102417. **=> contains results of the dissertation**

Franco P., Würtemberger U., Dacca K., Hübschle I., Beck J., Schnell O., Mader I., Binder H., Urbach H., Heiland D.H.SPectroscOpic prediction of bRain Tumours (SPORT): study protocol of a prospective imaging trial. BMC Med Imaging. 2020 Nov 23;20(1):123. doi: 10.1186/s12880-020-00522-y. **=> contains results of the dissertation**

Franco P., Delev D., Cipriani D., Neidert N., Kellner E., Masalha W., Mercas B., Mader I., Reinacher P., Weyerbrock A., Fung C., Beck J., Heiland D.H., Schnell O. Surgery for IDH1/2 wild-type glioma invading the corpus callosum. Acta Neurochir (Wien). 2020 Oct 23. doi: 10.1007/s00701-020-04623-z.

Heiland D.H., Ohle R., Cipriani D., **Franco P.**, Delev D., Behriger S.P., Kellner E., Petrova G., Neidert N., Mader I., Fariña Nuñez M.T., Urbach H., Sankowski R., Beck J., Schnell O. Characterization of longitudinal transformation of T2-hyperintensity in oligodendroglioma. BMC Cancer. 2020 Aug 27;20(1):818. doi: 10.1186/s12885-020-07290-6.

Delev D., Daka K., Heynckes S., Gaebelein A., **Franco P.**, Pfeifer D., Prinz M., Schnell O., Urbach H., Mader I., Beck J., Grote A., Becker A.J., Heiland D.H. Long-term epilepsy-associated tumors: transcriptional signatures reflect clinical course. Sci Rep. 2020 Jan 9;10(1):96. doi: 10.1038/s41598-019-56146-y. PMID: 31919458.

Fariña Nuñez M.T., **Franco P.**, Cipriani D., Neidert N., Behringer S.P., Mader I., Delev D., Fung C., Beck J., Sankowski R., Nicolay N.H., Heiland D.H., Schnell O. Resection of recurrent glioblastoma multiforme in elderly patients: a pseudo-

randomized analysis revealed clinical benefit. J Neurooncol. 2020 Jan;146(2):381-387. doi: 10.1007/s11060-020-03393-z.

Masalha W., Heiland D.H., Delev D., Fennell J.T., **Franco P.**, Scheiwe C., Mercas B.I., Mader I., Schnell O., Grauvogel J. Survival and Prognostic Predictors of Anaplastic Meningiomas. World Neurosurg. 2019 Nov;131:e321-e328. doi: 10.1016/j.wneu.2019.07.148.

Heiland D.H., Ravi V.M., Behringer S.P., Frenking J.H., Wurm J., Joseph K., Garrelfs N.W.C., Strähle J., Heynckes S., Grauvogel J., **Franco P.**, Mader I., Schneider M., Potthoff A.L., Delev D., Hofmann U.G., Fung C., Beck J., Sankowski R., Prinz M., Schnell O. Tumor-associated reactive astrocytes aid the evolution of immunosuppressive environment in glioblastoma. Nat Commun. 2019 Jun 11;10(1):2541. doi: 10.1038/s41467-019-10493-6.

Ravi V.M., Joseph K., Wurm J., Behringer S., Garrelfs N., d'Errico P., Naseri Y., **Franco P.**, Meyer-Luehmann M., Sankowski R., Shah M.J., Mader I., Delev D., Follo M., Beck J., Schnell O., Hofmann U.G., Heiland D.H. Human organotypic brain slice culture: a novel framework for environmental research in neuro-oncology. Life Sci Alliance. 2019 Jun 27;2(4):e201900305. doi: 10.26508/lsa.201900305.

Heynckes S., Daka K., **Franco P.**, Gaebelein A., Frenking J.H., Doria-Medina R., Mader I., Delev D., Schnell O., Heiland D.H. Crosslink between Temozolomide and PD-L1 immune-checkpoint inhibition in glioblastoma multiforme. BMC Cancer. 2019 Feb 1;19(1):117. doi: 10.1186/s12885-019-5308-y.

Delev D., Heiland D.H., **Franco P.**, Reinacher P., Mader I., Staszewski O., Lassmann S., Grau S., Schnell O. Surgical management of lower-grade glioma in the spotlight of the 2016 WHO classification system. J Neurooncol. 2019 Jan;141(1):223-233. doi: 10.1007/s11060-018-03030-w.

Heiland D.H., Haaker G., Watzlawick R., Delev D., Masalha W., **Franco P.**, Machein M., Staszewski O., Oelhke O., Nicolay N.H., Schnell O. One decade of glioblastoma multiforme surgery in 342 elderly patients: what have we learned? J Neurooncol. 2018 Nov;140(2):385-391. doi: 10.1007/s11060-018-2964-8.

Heiland D.H., Gaebelein A., Börries M., Wörner J., Pompe N., **Franco P.**, Heynckes S., Bartholomae M., Ó-hAilín D., Carro M.S., Prinz M., Weber S., Mader I., Delev D. Schnell O. Microenvironment-Derived Regulation of HIF Signaling Drives Transcriptional Heterogeneity in Glioblastoma Multiforme. Mol Cancer Res. 2018 Apr;16(4):655-668. doi: 10.1158/1541-7786.MCR-17-0680.

Kogias E., Klingler J.H., **Franco Jimenez P.**, Vasilikos I., Sircar R., Scholz C., Hubbe U. Incidental Durotomy in Open Versus Tubular Revision Microdiscectomy: A Retrospective Controlled Study on Incidence, Management, and Outcome. Clin Spine Surg. 2017 Dec;30(10):E1333-E1337. doi: 10.1097/BSD.0000000000000279.

Heiland D.H., Wörner J., Haaker G., Delev D., Pompe N., Mercas B., **Franco P.**, Gäbelein A., Heynckes S., Pfeifer D., Weber S., Mader I., Schnell O. The integrative metabolomic-transcriptomic landscape of glioblastome multiforme. Oncotarget. 2017 Jul 25;8(30):49178-49190. doi: 10.18632/oncotarget.16544.

Heynckes S., Gaebelein A., Haaker G., Grauvogel J., **Franco P.**, Mader I., Carro M.S., Prinz M., Delev D., Schnell O., Heiland D.H. Expression differences of programmed death ligand 1 in de-novo and recurrent glioblastoma multiforme. Oncotarget. 2017 Jun 28;8(43):74170-74177. doi: 10.18632/oncotarget.18819.

Heiland D.H., Staszewski O., Hirsch M., Masalha W., **Franco P.**, Grauvogel J., Capper D., Schrimpf D., Urbach H., Weyerbrock A. Malignant Transformation of a Dysembryoplastic Neuroepithelial Tumor (DNET) Characterized by Genome-Wide Methylation Analysis. J Neuropathol Exp Neurol. 2016 Apr;75(4):358-65. doi: 10.1093/jnen/nlw007.

Hubbe U., **Franco-Jimenez P.**, Klingler J.H., Vasilikos I., Scholz C., Kogias E. Minimally invasive tubular microdiscectomy for recurrent lumbar disc herniation. J Neurosurg Spine. 2016 Jan;24(1):48-53. doi: 10.3171/2015.4.SPINE14883. Epub 2015 Sep 18. PMID: 26384131.

Kogias E., **Franco Jimenez P.**, Klingler J.H., Hubbe U. Minimally invasive redo discectomy for recurrent lumbar disc herniations. J Clin Neurosci. 2015 Sep;22(9):1382-6. doi: 10.1016/j.jocn.2015.02.028. Epub 2015 Jun 27. PMID: 26122379.

Kogias E., **Jimenez P.F.**, Hubbe U. Microendoscopic lumbar discectomy: Technique and results of 188 cases. Indian J Orthop. 2015 Mar-Apr;49(2):262-3. doi: 10.4103/0019-5413.152551. PMID: 26015622; PMCID: PMC4436499.

Congress oral presentations

Franco P., Heiland D.H., Reinacher P., Masalha W., Mercas B., Schnell O. Integrative analysis of surgical, neurological and oncological outcomes of corpus callosum glioblastoma multiforme. 68. Jahrestagung der DGNC, Magdeburg, 14. May 2017.

Franco P., Daka K., Beck J., Schnell O., Urbach H., Heiland D.H. Spectroscopic Prediction Of bRain Tumors (SPORT) – a prospective imaging trial. 70. Jahrestagung der DGNC, Würzburg, 13. May 2019. doi: 10.3205/19dgnc022

Erklärung zum Eigenteil

Folgenden zwei Publikationen enthalten Ergebnisse der vorliegenden Dissertation:

1. **Franco P.,** Huebschle, I., Simon-Gabriel, C.P., Dacca, K., Schnell, O., Beck, J., Mast, H., Urbach, H., Wuerttemberger, U., Prinz, M., Hosp, J.A., Delev, D., Mader, I., Heiland, D.H. Mapping of Metabolic Heterogeneity of Glioma using MR-Spectroscopy. Cancers (Basel). 2021 May 17;13(10):2417. doi: 10.3390/cancers13102417.

2. **Franco P.,** Würtemberger U., Dacca K., Hübschle I., Beck J., Schnell O., Mader I., Binder H., Urbach H., Heiland D.H. SPectroscOpic prediction of bRain Tumours (SPORT): study protocol of a prospective imaging trial. BMC Med Imaging. 2020 Nov 23;20(1):123. doi: 10.1186/s12880-020-00522-y.

Das Konzipieren und Design der Studie, auf der beide Arbeiten basiert sind, wurden von meiner Betreuerin Prof. Dr. Irina Mader in Kollaboration mit PD Dr. Dieter Henrik Heiland entwickelt. Zudem wurden die Methoden-, Ergebnis- und Diskussionsteile der Manuskripte in der letztendlich veröffentlichten Form von PD Dr. Dieter Henrik Heiland mitverfasst.

Ich habe für beide Arbeiten die Patientenrekrutierung, die Sammlung und Analyse klinischer Daten, die Entwicklung der Segmentierungsapplikation, die manuelle Bildsegmentierung, die Analyse der Daten und die Einleitungs-, Methoden-, Ergebnis- und Diskussionsteile geschrieben. Die Segmentierungsapplikation wurde in Kollaboration mit Herrn Karam Dacca entwickelt. Die Segmentierung der MRS Bilder wurde mit Unterstützung von Frau Irene Hübschle durchgeführt. Der Algorithmus für die Prädiktion von Hirntumoren wurde in Kollaboration mit PD Dr. Dieter Henrik Heiland vom MILOLab entwickelt.

Die Abbildung 28 wurde mithilfe von Biorender erstellt: www.biorender.com

Eidesstattliche Versicherung

gemäß § 8 Absatz 1 Nr. 3 der Promotionsordnung der Universität Freiburg für die Medizinische Fakultät:

1. Bei der eingereichten Dissertation zum Thema handelt es sich um meine eigenständig erbrachte Leistung.

2. Ich habe nur die angegebenen Quellen und Hilfsmittel benutzt und mich keiner unzulässigen Hilfe Dritter bedient. Insbesondere habe ich wörtlich oder sinngemäß aus anderen Werken übernommene Inhalte als solche kenntlich gemacht. Niemand hat von mir unmittelbar oder mittelbar geldwerte Leistungen für arbeiten erhalten, die im Zusammenhang mit dem Inhalt der vorgelegten Dissertation stehen.

3. Die Ordnung der Albert-Ludwigs-Universität zur Sicherung der Redlichkeit in der Wissenschaft habe ich zur Kenntnis genommen und akzeptiert.

4. Die Dissertation oder Teile davon habe ich bislang nicht an einer Hochschule des In- oder Auslands als Bestandteil einer Prüfung oder Qualifikationsleistungen vorgelegt.

5. Die Richtigkeit der vorstehenden Erklärungen bestätige ich.

6. Die Bedeutung der eidesstattlichen Versicherung und die strafrechtlichen Folgen einer unrichtigen oder unvollständigen eidesstattlichen Versicherung sind mir bekannt.

Ich versichere an Eid statt, dass ich nach bestem Wissen die reine Wahrheit erklärt und nichts verschwiegen habe.

Freiburg, den 12.04.2021 Pamela Heiland

Danksagung

Ich danke ganz herzlich **Frau Prof. Dr. Irina Mader**, für die anspruchsvolle und interessante Promotions-Thematik und für die sehr engagierte Betreuung meiner Promotion.

Herrn **Prof. Dr. Horst Urbach** danke ich für die Möglichkeit, in seiner Klinik meine Promotionsarbeit anfertigen zu dürfen.

Ich bedanke mich herzlich bei **Prof. Dr. Oliver Schnell** für die Annahme der Zweitkorrektur dieser Arbeit und das energetische Mentoring in seiner Arbeitsgruppe.

Besonders danken möchte ich meinem Mann **PD Dr. Dieter Henrik Heiland**, denn dank seiner ständigen Unterstützung und Geduld habe ich meine wissenschaftliche Karriere realisiert. Für sein unermüdliches geduldiges Zuhören, auch wenn die Zeit knapp war, seine Hilfe mit Rat und Tat, für seine Rücksichtnahme und unbegrenzte Ermutigung werde ich für immer dankbar sein.

Ich möchte auch meinen Eltern **Pedro A. Franco** und **Marcela Jiménez** von ganzem Herzen danken, da sie mir immer mit Liebe und Freiheit unterstütz haben und mich bei jedem Vorhaben gefördert haben. Gracias a mis papás por ser los principales motores de mis sueños y siempre darme la seguridad y confianza para realizarlos.

Abschließend möchte ich meinem **Opa Hernando Jiménez** ganz herzlich danken, dass er immer in mir und meinen Fähigkeiten bedingungslos geglaubt hat und ein Vorbild und Motivationsquelle war und für immer sein wird. Te agradezco por siempre confiar en mí, creer en mí y en mis expectativas.